

Ly α Escape from $z \sim 0.03$ Star-Forming Galaxies: the Dominant Role of Outflows

Aida Wofford¹, Claus Leitherer¹ and John Salzer²

¹*Space Telescope Science Institute, 3700 San Martin Drive, Baltimore, MD 21218;*

`wofford@stsci.edu`

²*Astronomy Department, Indiana University, Swain West 408, 727 East Third Street, Bloomington, IN 47405*

ABSTRACT

The usefulness of H I Ly α photons for characterizing star formation in the distant universe is limited by our understanding of the astrophysical processes that regulate their escape from galaxies. These processes can only be observed in detail out to a few $\times 100$ Mpc. Past nearby ($z < 0.3$) spectroscopic studies are based on small samples and/or kinematically unresolved data. Taking advantage of the high sensitivity of *HST*'s COS, we observed the Ly α lines of 20 H α -selected galaxies located at $\langle z \rangle = 0.03$. The galaxies cover a broad range of luminosity, oxygen abundance, and reddening. In this paper, we characterize the observed Ly α lines and establish correlations with fundamental galaxy properties. We find seven emitters. These host young (≤ 10 Myr) stellar populations, have rest-frame equivalent widths in the range 1 – 12 Å, and have Ly α escape fractions within the COS aperture in the range 1 – 12 %. One emitter has a double-peaked Ly α with peaks 370 km s⁻¹ apart and a stronger blue peak. Excluding this object, the emitters have Ly α and O I $\lambda 1302$ offsets from H α in agreement with expanding shell models and LBG observations. The absorbers have offsets that are almost consistent with a static medium. We find no one-to-one correspondence between Ly α emission and age, metallicity, or reddening. Thus, we confirm that Ly α is enhanced by outflows and is regulated by the dust and H I column density surrounding the hot stars.

Subject headings: galaxies: evolution — galaxies: ISM — galaxies: starburst — galaxies: stellar content — ultraviolet: galaxies

1. INTRODUCTION

The potential of H I Ly α to identify young galaxies at high redshift was noted over 40 years ago by Partridge & Peebles (1967). Ly α corresponds to the $n = 1 - 2$ transition and is in principle the strongest emission line originating in an H II region. In the absence of dust, the Ly α /H α

line intensity ratio is expected to be in the range 7 – 12 for recombination theory cases B-A (Osterbrock & Ferland 2006), and the Ly α equivalent width, $EW(\text{Ly}\alpha)$, is expected to be in the range 100 – 300 Å for metallicities between $Z = 0.020 - 0.004$, a normal initial mass function, a constant star formation rate of $1 M_{\odot}/\text{yr}^{-1}$, and ages below 10 Myr (Verhamme et al. 2008). In the case of a single burst of star formation, the range of $EW(\text{Ly}\alpha)$ is $\sim 0 - 300$ under the same conditions. A few times $10^7 - 10^9$ yr after a burst of star formation, $EW(\text{Ly}\alpha)$ drops to zero (Charlot & Fall 1993; Valls-Gabaud 1993; Verhamme et al. 2008). The above predictions do not account for the underlying stellar contribution at Ly α . This contribution is not a concern in galaxies dominated by populations of O and early B stars. For reference, the mean Ly α equivalent width of the eight early and mid-O supergiants in Bouret et al. (2012) is ~ 1 Å. On the other hand, the correction can be significant for stellar populations dominated by A and late B stars. In addition, the above predictions do not account for the effects of Ly α radiation transfer in the medium surrounding the starburst. Due to its resonant nature, a Ly α photon is absorbed and re-emitted multiple times in H I. Resonant trapping reduces the mean free path of the Ly α photons increasing significantly their probability of being destroyed by dust, shifted in frequency, or transformed to two-photon emission. On the other hand, some effects are favorable to the escape of Ly α photons from galaxies. Neutral gas outflows Doppler-shift the Ly α photons from the optically thick line core to the optically thin line wings making it possible for some Ly α photons to escape (Kunth et al. 1998; Verhamme et al. 2006). Ly α photons may also escape through holes of sufficiently low dust and H I column densities (Giavalisco et al. 1996; Atek et al. 2009).

In spite of the various Ly α attenuation effects, today, star-forming galaxy candidates have been detected out to redshift $z \sim 10$ using various techniques. Galaxies with redshifts of $z \sim 2 - 5$ are detected via the drop-out technique based on the opacity at the Lyman-limit of the galaxy and the intervening intergalactic medium (IGM; Giavalisco 2002; Steidel et al. 2003; Shapley et al. 2003; Ouchi et al. 2004). Galaxies with $z \gtrsim 6$ are detected via the drop-out technique based on the opacity of the IGM at Ly α (Bouwens et al. 2007; Oesch et al. 2010; Bouwens et al. 2011a,b). Galaxies with $z \sim 2 - 7$ are also detected using deep narrow band surveys that target the Ly α emission-line (Cowie & Hu 1998; Hu et al. 1998, 2004, 2010; Rhoads et al. 2000; Ouchi et al. 2005, 2008; Taniguchi et al. 2005; Venemans et al. 2005; Nilsson 2007; Nilsson et al. 2009; Gronwall et al. 2007). Finally, galaxies at the highest redshifts are detected using gravitationally lensing clusters (Ota et al. 2012). Hundreds of galaxy candidates have been spectroscopically confirmed (Steidel et al. 1996; Rhoads et al. 2003; Dawson et al. 2007; Iye et al. 2006; Cowie et al. 2010; Bradač et al. 2012), and a few galaxies show impressively high rest-frame equivalent widths of $EW(\text{Ly}\alpha) \geq 150$ Å (Malhotra & Rhoads 2002; Shimasaku et al. 2006; Finkelstein et al. 2008), which could alternatively be due to the presence of an AGN (Charlot & Fall 1993).

In principle, after removing the observational and astrophysical biases, Ly α can be used for various applications. 1) To probe cosmic star formation rates (Kudritzki et al. 2000; Fujita et al. 2003; Gronwall et al. 2007; Zheng et al. 2012). 2) To probe the ionization fraction of the intergalactic medium during the final stages of re-ionization (Kashikawa et al. 2006; Malhotra & Rhoads 2006;

Dawson et al. 2007; Zheng et al. 2010; Bradač et al. 2012). 3) To probe the large-scale structure (Ouchi et al. 2001, 2003, 2004, 2005; Venemans et al. 2002, 2004; Wang et al. 2005; Stiavelli et al. 2005; Gawiser et al. 2007). 4) To identify potential hosts of population III star formation (Malhotra & Rhoads 2002; Shimasaku et al. 2006; Schaerer 2007). 5) And to constrain the nature and evolution of high-redshift galaxies Giavalisco (2002); Nilsson et al. (2007); Finkelstein et al. (2009); Shapley (2011); Malhotra et al. (2012); González et al. (2012). However, the use of Ly α as a cosmological tool is limited by our understanding of the astrophysical processes that regulate the escape of Ly α photons from galaxies and affect them on their way to telescopes.

The Ly α escape problem can be approached from two complementary angles, doing statistically significant studies of the global properties of the sources and their cosmological context, or studying individual sources in detail. The former is better done in the distant universe, whereas the latter can only be accomplished locally, where the effect of the intergalactic medium is a non-issue, the kinematical and spatial resolutions are higher, and ancillary data is abundant. The challenges of studying Ly α locally are the necessity of a UV space-based observatory optimized for studying Ly α ; contamination with the geocoronal Ly α line, which saturates the spectra at very low redshift; and contamination with the Milky Way Galaxy Ly α -line trough. Indeed, the interstellar H I in our Galaxy produces a damped absorption along many sight-lines, which hides the potential Ly α line from star-forming galaxies with redshifts below a few $\times 100$ km s $^{-1}$.

There are several observational Ly α studies of galaxies at low-redshift ($z < 0.3$). Giavalisco et al. (1996) studied low resolution spectra of 21 galaxies taken with the *International Ultraviolet Explorer (IUE)* and studied the effects of reddening and metallicity on $EW(\text{Ly}\alpha)$, and $\text{Ly}\alpha/\text{H}\beta$. They found no correlation between these quantities and the UV extinction, the Balmer decrement, or the oxygen abundance. They concluded that rather than the amount of dust, the ISM geometry determines the Ly α escape fraction. Unfortunately, the spectral resolution of *IUE* is insufficient to study the effect of gas outflows on the Ly α escape. Kunth et al. (1998) studied high-dispersion *Hubble Space Telescope (HST)* GHRS spectra of eight nearby H II galaxies. They found four emitters, all of which have a velocity offset between the H I and the H II gas of up to 200 km s $^{-1}$, while the non-emitters show no velocity offset. However, their study suffers from small number statistics. Scarlata et al. (2009) analyzed the optical spectra of a sample of 31 $\langle z \rangle \sim 0.3$ Ly α emitters identified by Deharveng et al. (2008) in low resolution ($\sim 8 \text{ \AA}$) *Galaxy Evolution Explorer (GALEX)* data. They tried to reproduce the stellar-absorption corrected $\text{Ly}\alpha/\text{H}\alpha$ and $\text{H}\alpha/\text{H}\beta$ ratios using different dust geometries and assumptions for the Ly α scattering in H I. They found that the ratios are well reproduced by a clumpy dust distribution, while a uniform dust screen model results in $\text{Ly}\alpha/\text{H}\alpha$ larger than the case B recombination theory value. Unfortunately, the spectral resolution of *GALEX* is insufficient for kinematical studies, and the latter authors were unable to assess the relative importance of dust geometry and outflows. Atek et al. (2009) used a 3D Ly α radiation transfer code to model *HST* observations of the very metal-poor dwarf galaxy I Zw 18, which shows Ly α in absorption. Their analysis shows that it is possible to transform a strong Ly α emission of $EW(\text{Ly}\alpha) \approx 60 \text{ \AA}$ into a damped absorption, even with low extinction, if the H I column density

is large. Finally, Östlin et al. (2009) used *HST* to produce Ly α , H α , and UV continuum maps of six galaxies covering a wide range in luminosity and metallicity, including known Ly α emitters and non-emitters. They found that the bulk of Ly α emerges in a diffuse component resulting from scattering events. They also found the simultaneous presence of Ly α in emission and absorption within spatial scales ranging from a few $\times 10$ pc to a few $\times 100$ pc.

Although these studies have addressed main factors affecting the Ly α escape, we still do not understand the relative importance of starburst phase, gas kinematics, gas geometry, and dust extinction, in determining the profile and strength of the Ly α line from star-forming galaxies. We took advantage of the high sensitivity and medium resolution of the Cosmic Origins Spectrograph (COS) aboard *HST* in order to obtain Ly α spectroscopy of a sample of 20 galaxies located a mean redshift of 0.03 and covering a broad range of luminosity, oxygen abundance, and reddening. We used these and ancillary data for establishing correlations between Ly α and fundamental galaxy properties. In section 2 we describe the sample, the observations, and the ancillary data; in section 3 we present our analysis; in section 4 we discuss our results; and in section 5 we summarize and conclude.

2. SAMPLE, OBSERVATIONS, AND ANCILLARY DATA

2.1. Sample

The galaxies in our sample were H α -selected from the Kitt Peak International Spectroscopic Survey data release (KISSR¹, Salzer et al. 2001). The sample is composed of 12 irregular and eight spiral galaxies distributed in the redshift range $z = 0.02 - 0.06$. At these redshifts, we avoid contamination with the geocoronal and Milky Way (MW) Ly α lines. We cover a factor of three in redshift, which makes it possible to study the effect of distance on the observed properties of Ly α . In addition, we cover a broad range in oxygen abundance, $12 + \log(\text{O}/\text{H}) = 7.9 - 9.1$, which makes it possible to study the effect of metallicity² on the Ly α escape. Metallicity is expected to correlate with the dust content, and dust destroys Ly α photons. We also cover a wide range in H α equivalent width, $EW(\text{H}\alpha) = 27 - 578 \text{ \AA}$. The value of $EW(\text{H}\alpha)$ is sensitive to the starburst evolutionary phase and to the initial mass function (IMF), e.g., see Leitherer et al. (1999). Finally, we cover over an order of magnitude in *GALEX* (Martin et al. 2005) FUV continuum luminosity, $\log L(1500) = 39.0 - 40.2 \text{ erg s}^{-1} \text{ \AA}^{-1}$ (uncorrected for reddening). For a given star formation history (SFH), age, and IMF, $L(1500)$ is proportional to the stellar mass in the population dominating the FUV emission of the galaxy. Therefore, $L(1500)$ can be used to determine the star formation rate of this population ($\text{SFR} = \text{stellar mass} / \text{time since beginning of star formation}$). Table 1 summarizes the properties of the sample. The morphological types are based on SDSS images. The

¹The R in “KISSR” stands for data with red spectra, i.e., from 6400 – 7200 Å

²In this paper, metallicity is the mass ratio of all elements excluding H and He to all elements.

H α equivalent widths are from the SDSS spectra when available or from the KISS data otherwise, as indicated in column (10) of Table 1.

2.2. Spectral Class of the Galaxies

We are interested in galaxies where the principal photoionization source is the strong UV radiation from OB stars. This helps in the interpretation of the observed Ly α properties because we do not need to worry about non-stellar ionizing sources such as active galactic nuclei (AGNs), which account for some of the high Ly α EWs at $z > 2$ (Charlot & Fall 1993; Zheng et al. 2010), and low-ionization nuclear emission-line regions (LINERs), whose nature is not well understood (Tanaka 2012). We verified the spectral class of our galaxies using the so-called BPT diagnostic diagram (Baldwin, Phillips & Terlevich 1981). This was not possible for KISSR 271, for which an optical spectrum was unavailable. As Figure 1 shows, most galaxies are dominated by star formation, but KISSR 1084 may be of composite type.

2.3. Observations

Our observations are part of COS-GTO programs 11522 and 12027 (P.I. J. Green). Descriptions of the COS and its on-orbit performance can be found in Osterman et al. (2011). We used one orbit with *HST* to observe the brightest FUV knot detected by *GALEX* in each galaxy. We acquired the targets using the ACQ/IMAGE mode and mirror A. Therefore, we obtained two images of each galaxy in the observed-frame wavelength range 1700 – 3200 Å. One after the initial telescope pointing, and the second after the final telescope pointing. We then used the G130M grating to obtain a spectrum of each target in the observed-frame wavelength range 1138–1457 Å. We achieved continuous wavelength coverage by using central wavelengths, $\lambda 1291$ and $\lambda 1318$ at the default focal plane offset position (FP-POS=3). Table 2 lists the epochs and exposure times corresponding to these central wavelengths. The spectra were taken through the circular Primary Science Aperture (PSA), which is 2.5" in diameter. They contain the aberrated light from objects located up to 2" or up to 0.9 – 2.4 kpc from the aperture's center, depending on the distance to the galaxy. The data were processed with CALCOS v2.13.6 and combined with the custom IDL co-addition routine described in Danforth et al. (2010).

2.4. COS Images

Figure 2 shows the NUV target acquisition (TA) confirmation images of the galaxies with the COS aperture overlaid. The center of the aperture is indicated by the small black cross. In 12 cases, a clear source centroid associated with young star clusters is present. However, in eight cases, there is no clear centroid of the emission. This is due to the short exposure times of the TA

Table 1. Sample Properties

Galaxy	Morph.	z	d	M _B	E(B-V) _G	12+log(O/H)	EW(H α)	log L ₁₅₀₀	Note
(1)	(2)	(3)	Mpc	mag	mag	dex	Å	erg/s/Å	(10)
40	Irr	0.026	112	-18.0	0.03	8.18	58	39.29	1
108	Irr	0.024	101	-17.6	0.01	8.17	108	39.22	1
178+	Irr	0.057	246	-20.1	0.01	8.52	100	40.13	1
182	Irr	0.022	96	-17.8	0.01	8.34	114	39.33	1
218	S	0.021	90	-19.4	0.01	8.87	66	39.65	1
242*	Irr	0.038	162	-19.4	0.01	8.38	435	40.25	1
271*	Irr	0.023	97	-17.6	0.02	8.39	29	39.13	2
298*	S	0.049	210	-20.0	0.02	9.07	51	40.06	1
326*	S	0.028	120	-20.0	0.02	8.74	78	39.65	2
1084*	S	0.032	137	-20.5	0.05	8.79	87	39.7	1
1567*	S	0.045	194	-20.0	0.02	8.75	29	40.18	2
1578*	Irr	0.028	120	-19.6	0.02	8.14	576	40.29	1
1637	Irr	0.035	149	-19.6	0.01	8.55	34	39.92	1
1785–	Irr	0.021	90	-17.6	0.01	7.99	199	39.07	1
1942	Irr	0.039	169	-19.3	0.03	8.59	25	39.83	1
2019	Irr	0.034	146	-17.9	0.02	7.96	465	39.48	1
2021	S	0.04	171	-19.6	0.02	8.79	79	39.93	1
2023	S	0.036	155	-19.4	0.02	9.00	58	39.77	1
2110	Irr	0.025	108	-17.3	0.01	7.86	511	39.36	2
2125	S	0.025	108	-18.7	0.01	8.76	85	39.31	1
Min	...	0.021	90	-20.5	0.01	7.86	25	39.07	...
Max	...	0.057	246	-17.3	0.05	9.07	576	40.29	...

Note. — (1) KISSR ID. We mark the Ly α emitters with asterisks and the furthest/nearest galaxies with plus/minus signs. The last two rows give the minimum and maximum values in each column. (2) Morphological type. S=spiral. Irr=irregular. (3) Redshift of H α line. (4) Distance computed from the redshift using $d = cz/H_0$, where c is the speed of light, z is the redshift, and we adopt $[\Omega_\lambda, \Omega_M, H_0] = [0.7, 0.3, 70 \text{ km s}^{-1} \text{ Mpc}^{-1}]$. (5) Absolute blue magnitude. (6) Color excess based on the Milky Way extinction maps of Schlegel et al. (1998) and the reddening law with $R_V = 3.1$ of Fitzpatrick (1999). (7) Oxygen abundance derived as in Salzer et al. (2005). (8) H α equivalent width. (9) Luminosity at 1500 Å from *GALEX*, uncorrected for reddening. (10) Source of the ancillary optical spectrum. 1=SDSS. 2=Same as in Salzer et al. 2005.

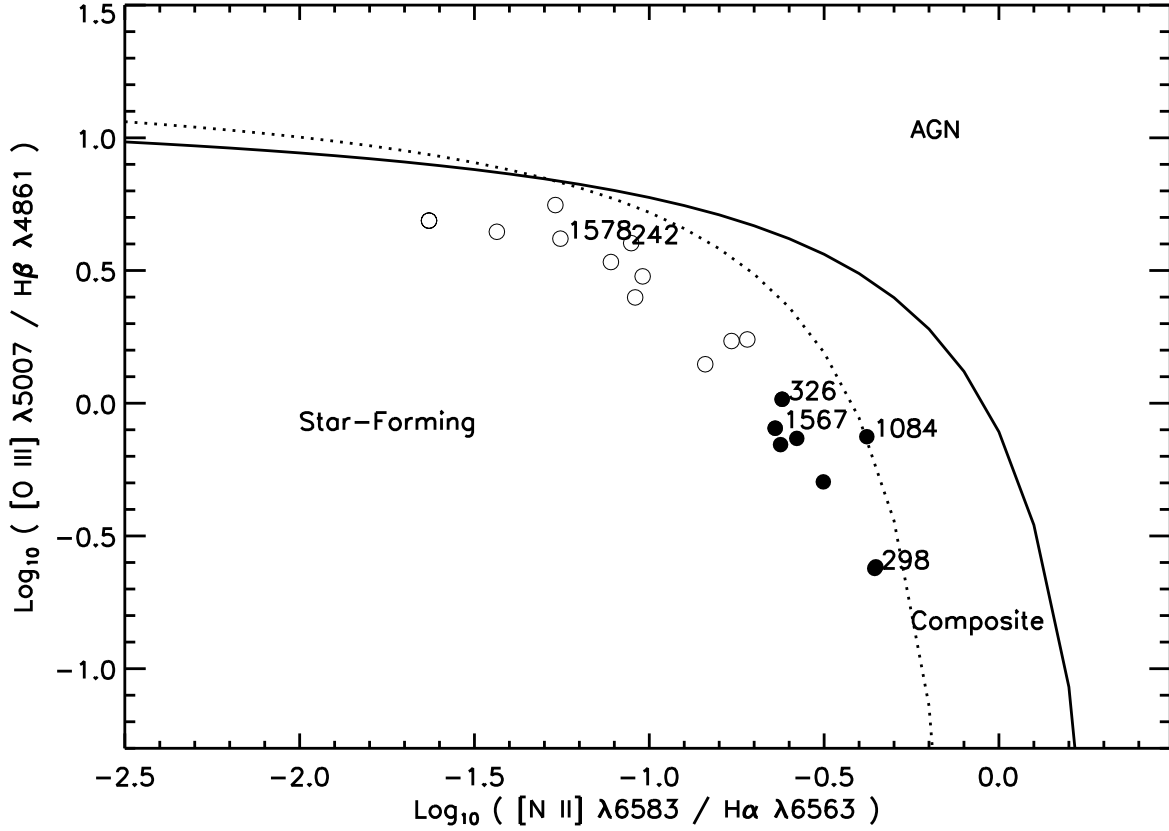


Fig. 1.— Baldwin, Phillips & Terlevich diagnostic diagram of the spiral (filled symbols) and irregular (open symbols) galaxies in our sample. We adopt the scheme of Kewley et al. (2006), where the principal excitation mechanism in the galaxy is star formation if the galaxy lies below the dotted curve, an AGN if the galaxy lies above the solid curve, and a mixture of star formation and Seyfert nucleus, or star formation and LINER, if the galaxy lies between the dotted and solid curves. The dotted curve corresponds to equation 1 in Kauffmann et al. (2003). The solid curve corresponds to equation 5 in Kewley et al. (2001). The symbols of the Ly α emitters are labeled with the KISSR ID of the galaxy.

images and in two cases, i.e., for KISSR galaxies 40 and 1567, to TA failures. In spite of the TA failures, spectra were taken. The galaxies that turned out to have net Ly α emission are marked with asterisks. Hereafter, we will call the latter galaxies the emitters. Note that emitters KISSR 271, 326, and 1567, do not show source centroids. Also note that in spite the TA failure, KISSR 1567 turned out to be an emitter. This is in agreement with the finding of Östlin et al. (2009) that the Ly α emission is not necessarily coincident with regions of high FUV surface brightness.

2.5. Ancillary Images

We obtained information about the morphology and orientation of the galaxies from archival images. At the time of our analysis, there were no *HST* images available for our targets. The galaxies were imaged by *GALEX* in the FUV at low spatial resolution ($\sim 0.5''$). Unfortunately, in these images, the galaxies look like large blobs. However, we found useful Sloan Digital Sky Survey (SDSS, York et al. 2000) images of all the targets in our sample. These are shown in Figure 3, where we have overlaid the COS footprint at the approximate location of the telescope pointing and marked the emitters with asterisks.

Figure 3 shows that most spiral galaxies in our sample have low inclinations except KISSR 2125. While some low-inclination spirals have Ly α in emission, others don't. KISSR 1084, the spiral of composite spectral class is an emitter, and as expected, the highly inclined spiral is a non-emitter. Our two most metal-poor irregulars, KISSR 2019 and 2110, are Ly α absorbers, but irregulars KISSR 242 and 1578 are Ly α emitters. In summary, there are emitters and absorbers among both morphological types. Finally, note that the COS aperture only covers an area of 0.9 – 2.4 kpc in radius, depending on the distance to the galaxy. This needs to be considered when comparing with Ly α observations at higher redshifts, since at higher redshift, more of the galaxy is enclosed within the aperture and Östlin et al. (2009) found that the bulk of the Ly α photons from nearby galaxies are in the diffuse halo.

2.6. Ancillary Spectra

We used ancillary optical spectroscopy of the galaxies for determining their redshift, spectral class, metallicity, reddening, SFR, and Wolf-Rayet (WR) star content. Sixteen targets have spectra from the SDSS seventh data release (Abazajian et al. 2009). The SDSS spectra are of higher spectral resolution than the KISSR spectra, and they were taken through a circular fiber of 3'' in diameter that closely matches the size of the COS aperture. The difference between the SDSS and the COS pointings is relevant to the interpretation of the Ly α /H α ratio, and to the comparison of the strength of Ly α and the value of $EW(H\alpha)$. Indeed, the COS aperture encompasses only a portion of each galaxy. Table 3 lists the KISSR identifier (Column 1, the emitters are marked with asterisks), the

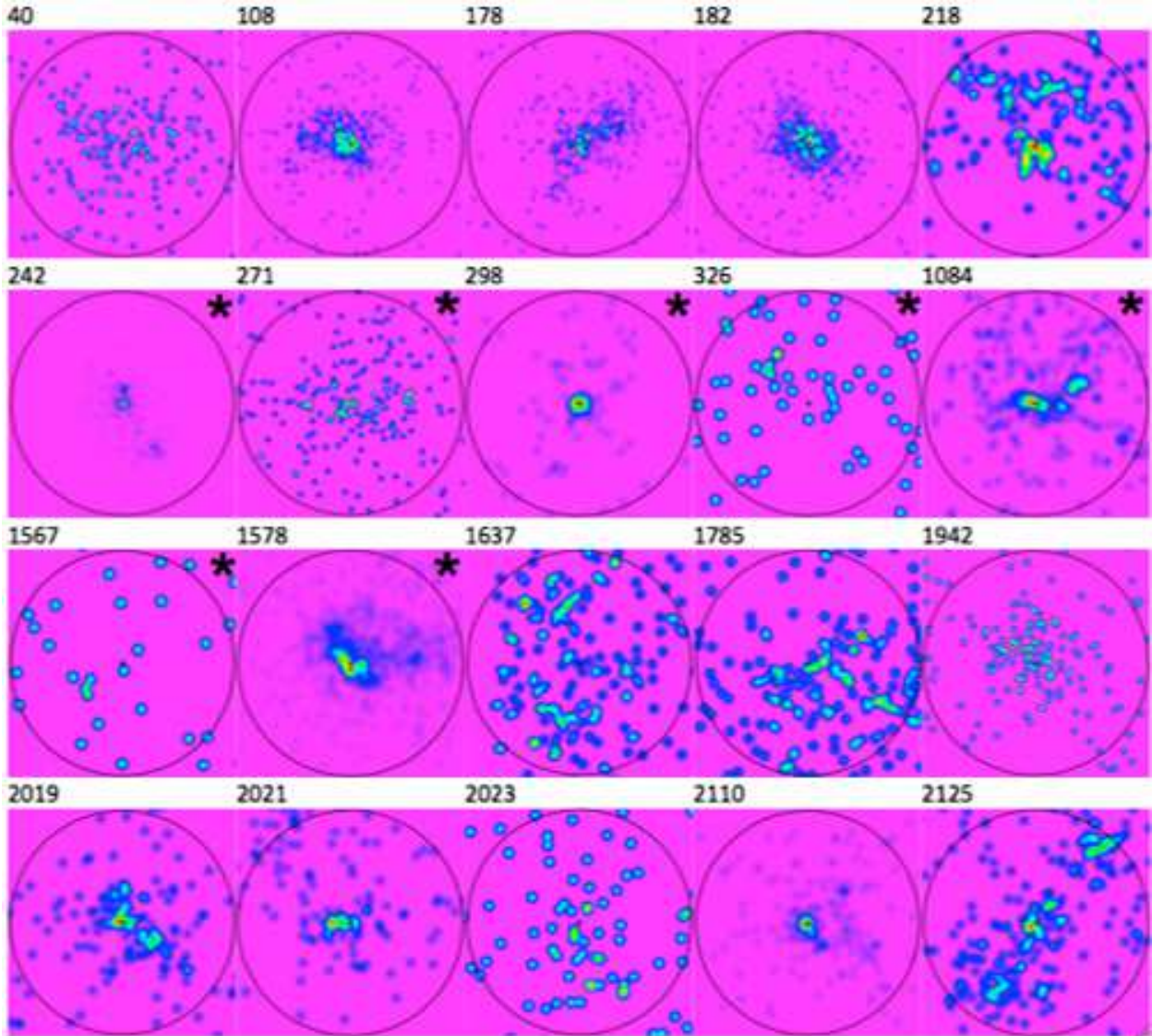


Fig. 2.— Near-ultraviolet (1700 – 3200 Å) COS TA confirmation images. North is up and east is to the left. The numbers are the galaxy identifiers. The circles represent the 2.5" in diameter COS PSA aperture. The emitters are marked with asterisks. In the rainbow scale, red represents the region of maximum counts, while pink represents regions of low counts.

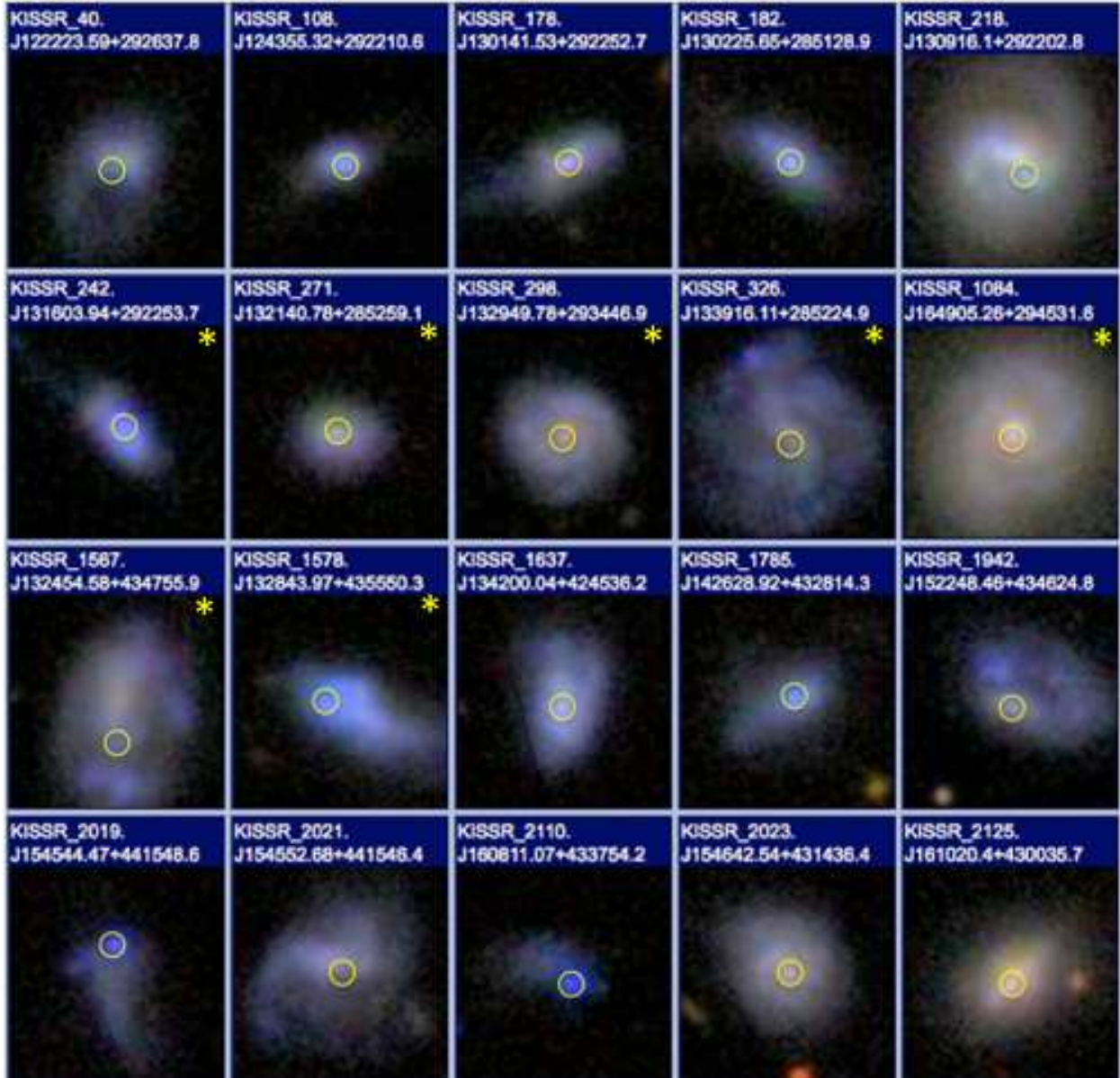


Fig. 3.— Sloan Digital Sky Survey 25" x 25" u-, g-, r-, i-, and z-band composite images of the galaxies. The KISSR and SDSS galaxy identifiers are provided. North is up and east is to the left. The Ly α emitters are marked with asterisks. The yellow circles show the COS footprint and pointing.

right ascension (RA, J2000) and declination (DEC, J2000) of the first *HST* pointing³ (Columns 2 and 3), the RA and DEC of the SDSS spectroscopic pointing (Columns 4 and 5), and the difference between the COS and the SDSS pointings (Columns 6-8). As Table 3 shows, on average, the SDSS pointings are within 0.3" of the COS initial pointings, with a standard deviation of 0.4". Since the diameter of the COS aperture is 2.5", we do not expect the difference in pointings to constitute a major issue. For KISSR galaxies 326, 1567, and 2110, which do not have SDSS spectra, we were able to recover the optical 2"-wide slit spectra of Jangren et al. (2005). Unfortunately, we do not have an optical spectrum for KISSR galaxy 271.

3. ANALYSIS

3.1. Wavelength Zero Point and Effective Spectral Resolution

The COS spectra include the intrinsic lines Ly α and a number of low-ionization (LIS) and higher-ionization interstellar lines. We are interested in comparing the offsets of these lines with respect to H α . This is for two reasons. First, as mentioned in the introduction, velocity offsets between the HII gas traced by H α and the HI gas traced by the LIS lines have been showed to favor the escape of Ly α from galaxies. Second, in expanding-shell radiation transfer models the Ly α emission line is redshifted to a few times the shell expansion velocity (e.g., Verhamme et al. 2006). A similar offset is observed at high redshift when comparing the Ly α redshift to the blueshift of the LIS lines, which give the expansion velocity (e.g. Shapley et al. 2003). Thus, offset measurements are useful for establishing how the Ly α strength relates to the interstellar gas kinematics and for constraining radiation transfer models. The accuracy of the velocity offset measurements depends on the accuracy of the wavelength zero point and on the effective spectral resolution of the data.

In ultraviolet spectroscopic studies of low-redshift galaxies, it is common to use geocoronal emission lines to check if the wavelength zero point is shifted due to instrumental effects, and Milky-Way metal absorption lines to check if the wavelength zero point is shifted due to the asymmetry of the target in the aperture (e.g., see Kriss et al. 2011). Figures 4-8 show the COS spectra of the galaxies. They are contaminated with some or all of the geocoronal emission lines H I λ 1216, N I λ 1200, and/or O I λ 1302, 1305; and with the Milky Way (MW) absorption lines, Si II λ 1190, 1193, 1260, 1304, Si III λ 1206, O I 1302, 1305, and/or C II λ 1334, 1336. We measured the centroids of the contaminating lines using a custom routine developed by COS science team member K. France. The routine takes into consideration the COS line spread function. Table 4 lists the mean wavelength offsets of the geocoronal and MW lines. We find that the mean velocity offsets of the geocoronal and MW lines are in the ranges -33 to 18 km s $^{-1}$ and -1 to 110 km s $^{-1}$, respectively.

³The position of the final *HST* pointing is not recorded in the standard output from CALCOS v2.13.6. It is expected to be within 0.3" of the initial pointing based on results of blind pointing exposures.

Table 2. Epochs and Exposure Times of G130M Observations

Galaxy	Start Time 1291 Å	Start Time 1318 Å	Exp. Time (s) 1291 Å	Exp. Time (s) 1318 Å
(1)	(2)	(3)	(4)	(5)
40	2011/06/11 02:07:49	2011/06/11 03:26:08	1105	1105
108	2011/07/31 04:47:42	2011/07/31 05:09:24	1105	1105
178	2011/06/17 20:55:13	2011/06/17 21:16:55	1105	1105
182	2011/07/26 08:13:51	2011/07/26 08:35:33	1105	1105
218	2010/02/23 07:33:10	2010/02/23 09:09:06	1111	1111
242	2009/12/26 23:56:45	2009/12/27 00:18:33	1111	1111
271	2011/05/07 17:41:45	2011/05/07 18:03:27	1105	1105
298	2010/01/01 12:41:22	2010/01/01 13:03:04	1105	1105
326	2011/04/22 13:36:31	2011/04/22 13:58:13	1105	1105
1084	2010/02/05 05:13:19	2010/02/05 05:35:01	1105	1105
1567	2010/08/13 05:09:19	2010/08/13 05:31:46	1150	1150
1578	2010/02/18 22:07:27	2010/02/18 22:29:57	1153	1153
1637	2009/10/24 09:51:17	2009/10/24 10:13:44	1150	1150
1785	2011/08/09 10:38:26	2011/08/09 11:00:55	1142	1142
1942	2011/06/13 22:46:13	2011/06/13 23:08:28	1128	1128
2019	2011/06/19 15:57:20	2011/06/19 16:19:49	1142	1142
2021	2009/11/14 00:02:53	2009/11/14 00:25:17	1147	1147
2023	2011/06/16 14:29:53	2011/06/16 14:52:08	1128	1128
2110	2011/06/16 16:16:21	2011/06/16 16:38:50	1142	1142
2125	2011/06/16 17:52:32	2011/06/16 18:15:01	1142	1142

Table 3. Comparison of COS and SDSS Pointings

Galaxy	COS RA	COS DEC	SDSS RA	SDSS DEC	Δ RA	Δ DEC	Δ_{tot}
(1)	deg	deg	deg	deg	deg	deg	arcsec
(1)	(2)	(3)	(4)	(5)	(6)	(7)	(8)
40	185.59833	29.44383	185.59825	29.44394	8E-05	-1E-04	0.49
108	190.98042	29.36964	190.98044	29.36961	-2E-05	3E-05	0.13
178	195.42306	29.38118	195.42304	29.38135	2E-05	-2E-04	0.62
182	195.60688	28.85808	195.60688	28.85807	-5E-06	1E-05	0.05
218	197.31725	29.36739	197.31703	29.36766	2E-04	-3E-04	1.24
242*	199.01625	29.38161	199.01632	29.38169	-7E-05	-8E-05	0.38
271*	200.42000	28.88308
298*	202.45746	29.57972	202.45748	29.57972	-2E-05	2E-06	0.08
326*	204.81708	28.87361
1084*	252.27192	29.75878	252.27195	29.75878	-3E-05	-2E-06	0.12
1567*	201.22750	43.79889
1578*	202.18354	43.93069	202.18357	43.93070	-3E-05	-6E-06	0.10
1637	205.50002	42.76004	205.50038	42.76000	-4E-04	4E-05	1.30
1785	216.62029	43.47083	216.62029	43.47082	2E-06	1E-05	0.05
1942	230.70200	43.77347	230.70197	43.77347	3E-05	2E-06	0.11
2019	236.43554	44.26439	236.43552	44.26439	2E-05	-1E-06	0.08
2021	236.46992	44.26322	236.46991	44.26322	7E-06	2E-06	0.03
2023	236.67746	43.24367	236.6774	43.24359	6E-05	8E-05	0.35
2110	242.04625	43.63175
2125	242.58508	43.00975	242.58507	43.00975	1E-05	0E+00	0.05

The MW lines arise from absorption in halo clouds that may have non-negligible heliocentric velocities. For this reason, we analyzed the HI 21 cm emission from intermediate velocity clouds (IVCs) along the lines of sight to our targets. The data are from the LAB HI survey (Kalberla et al. 2005). In Figure 9 we compare the centroids of the HI IVC emission lines and the MW Si II $\lambda 1990$ absorptions. The Si II absorptions are corrected for the wavelength offset given by the geocoronal lines. The HI 21 cm emission is the mean within the radio beam at each velocity. We chose Si II $\lambda 1990$ because it is the only MW line that is not blended with other lines for any of the targets. The HI component near 0 km s^{-1} originates in the MW disk. We find that the maximum IVC cloud velocity is $\sim -50 \text{ km s}^{-1}$ in the local standard of rest frame (e.g., KISSR 40, 1567, and 1578). Although the comparison between the 21 cm emission and the COS data is difficult in cases where the signal to noise of the COS data is low, in general, the 21 cm emission and the Si II absorption overlap. However, in some of the highest signal-to-noise cases (e.g., KISSR 242, 1578, 2019, and 2110), the minimum of the absorption is blueward of the bluest 21 cm emission peak. Note that the radio beam is large in comparison with the COS aperture, which makes this wavelength calibration method imperfect. Since large offsets between the 21 cm and the COS data are unlikely to be due to shifts in the wavelength zero point, we decided to only correct the COS data for the small shift in the geocoronal lines.

Regarding the spectral resolution, the more extended the source, the worse the effective spectral resolution, and the worse the accuracy in the determination of line centroids. Figure 2 shows that some targets are more extended than others. We used the MW lines Si II $\lambda 1190$, 1193, 1260, Si III $\lambda 1206$, and/or C II $\lambda 1334$ for determining the effective spectral resolution of the COS spectra. The dispersion of the G130M grating is $9.97 \text{ m}\text{\AA}/\text{pix}$ and the resolution element is 6 pixels. Therefore, the nominal resolution is 0.06 \AA or $\sim 16 \text{ km s}^{-1}$. The effective spectral resolution of each spectrum is given by the FWHM of the MW absorption lines. For each galaxy, Column 4 of Table 4 lists the mean effective spectral resolution. The mean FWHM of the MW lines is in the range $74 - 305 \text{ km s}^{-1}$. We can derive the centroids of the LIS lines with an accuracy of a tenth of the effective spectral resolution, as long as the signal to noise ratio is sufficient.

3.2. Ly α and ISM Kinematics

Here we present the velocity offsets of the intrinsic lines mentioned in the previous section. Figure 10 shows the Ly α profiles of the galaxies. Seven objects have net Ly α emission (emitters), eleven objects have damped Ly α absorptions (absorbers), and two objects, KISSR 2021 and 2023 have noisy Ly α profiles blended with MW lines and that appear to be in absorption with perhaps some Ly α emission. We measured the Ly α centroids as follows. For the emitters, the centroid is the point of maximum Ly α flux. For the absorbers, we used the center of the best-fit Voigt profile. The fits to the Ly α absorptions were done by eye using a custom routine written by J. Tumlinson. We overlay the Voigt profiles in Figure 10.

Excluding KISSR 298, the emitters have P-Cygni like profiles with the emission component

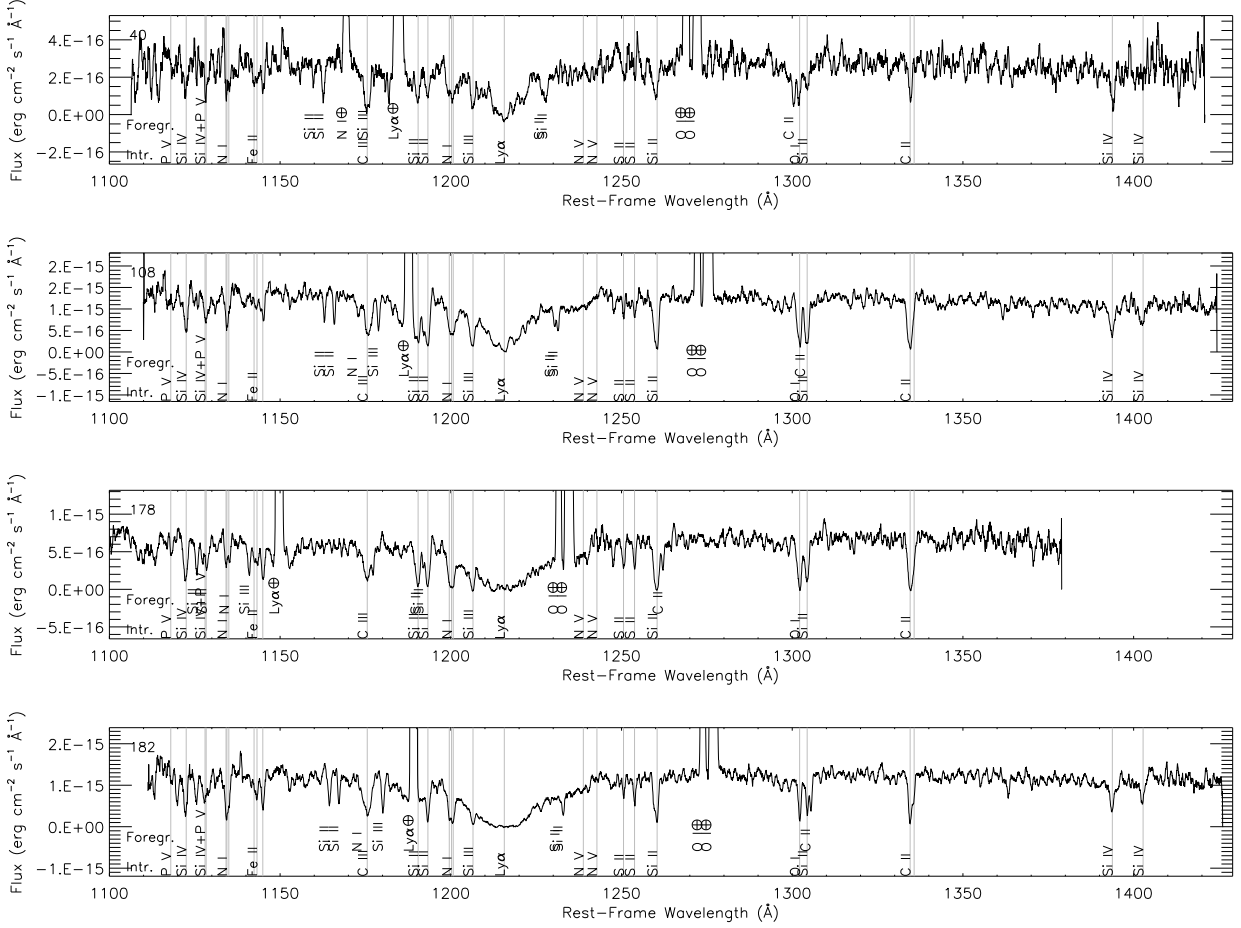


Fig. 4.— COS spectra of galaxies KISSR 40 , 108, 178, and 182 from top to bottom (KISSR ID provided on the upper left of each panel). The spectra are corrected for the redshift and uncorrected for the reddening. They were first binned to 16 km s^{-1} (nominal resolution of the COS spectra) and then smoothed for clarity. We identify foreground (Foregr.) and intrinsic (Intr.) lines at the bottom of each panel. Geocoronal lines are marked with an encircled plus. The intrinsic lines are marked with vertical gray lines. We did not clip the geocoronal lines in order to show the extent to which they affect the profiles of nearby lines.

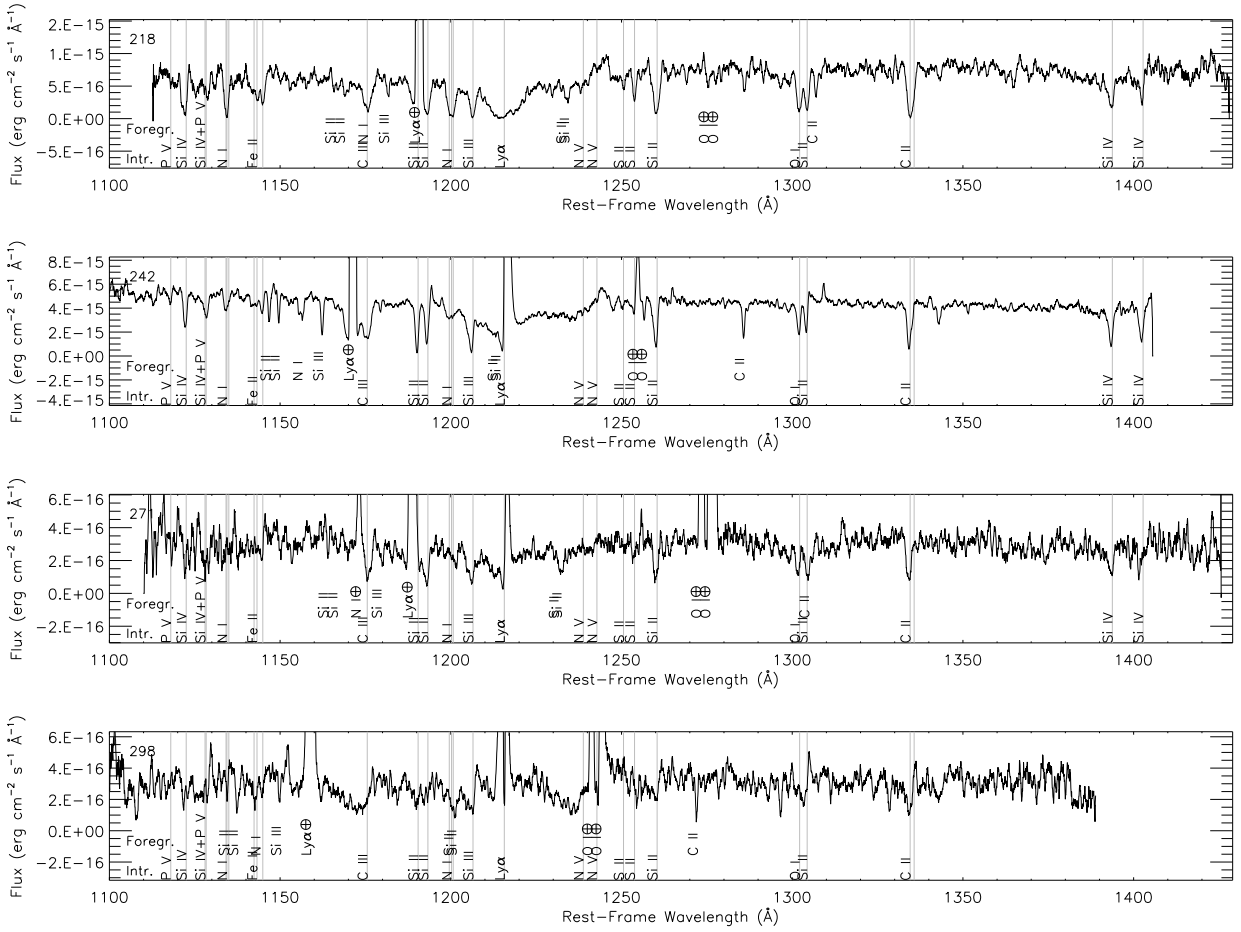


Fig. 5.— Similar to Figure 4 but for galaxies KISSR 218, 242, 271, and 298 from top to bottom.

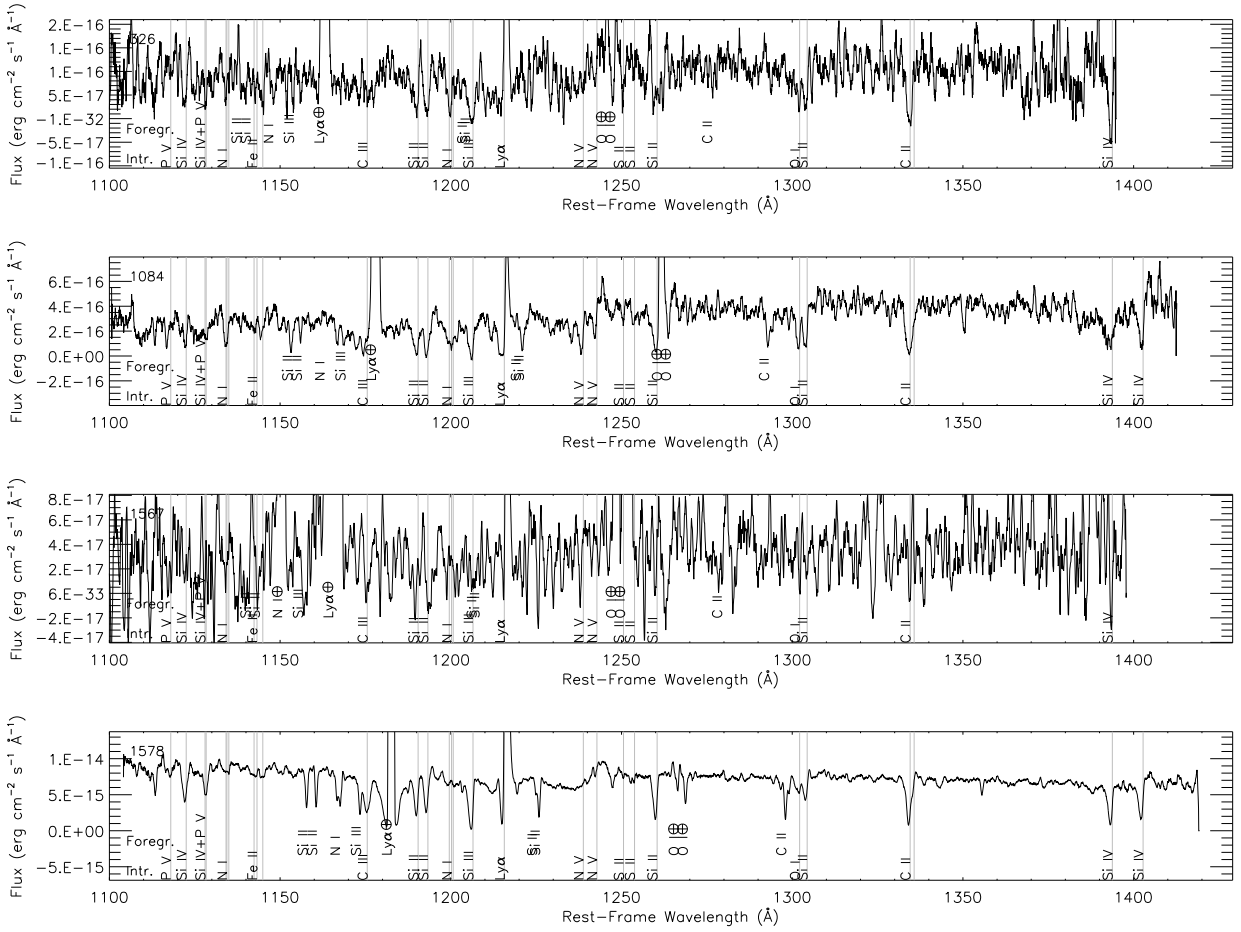


Fig. 6.— Similar to Figure 4 but for galaxies KISSR 326, 1084, 1567, and 1578 from top to bottom.

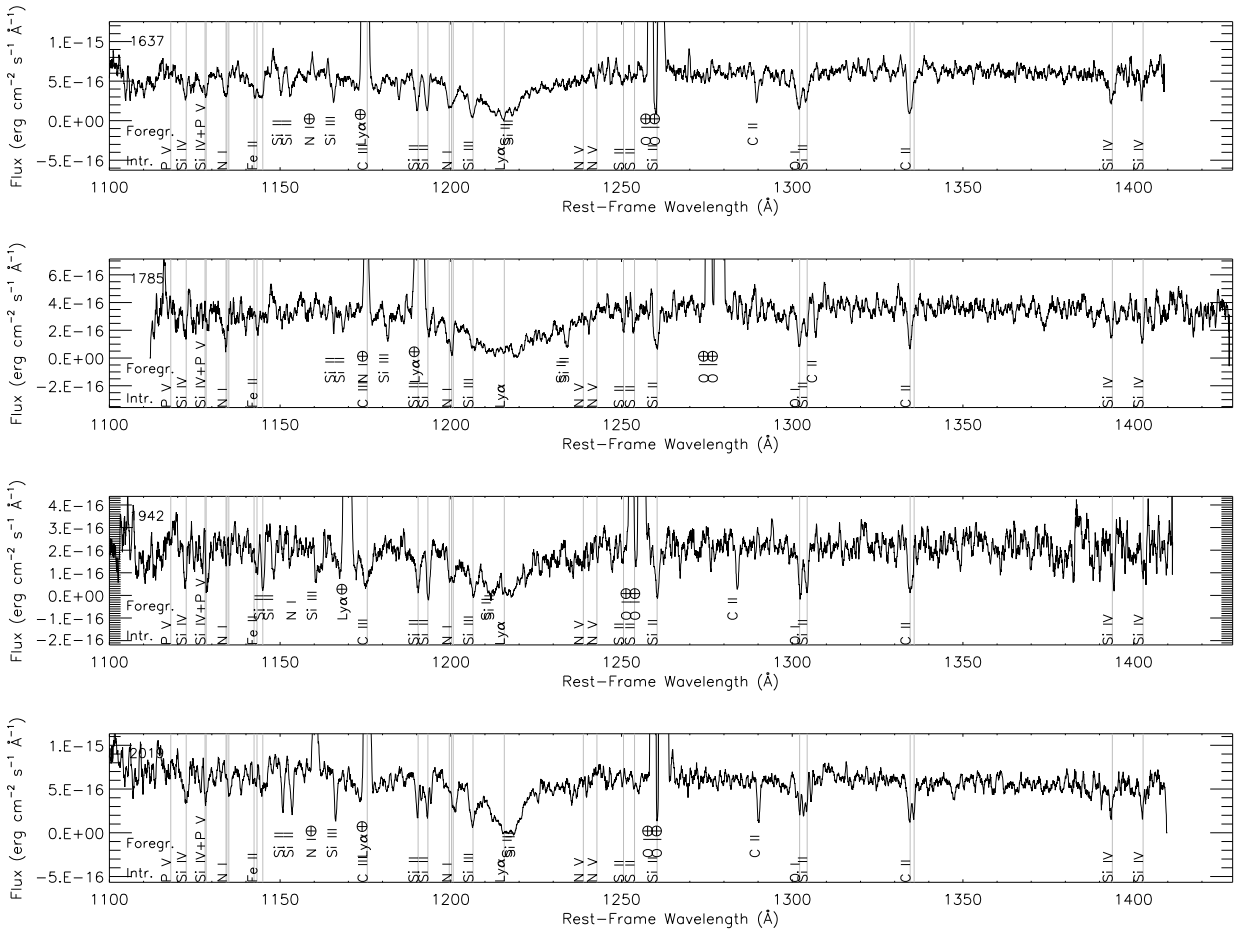


Fig. 7.— Similar to Figure 4 but for galaxies KISSR 1637, 1785, 1942, and 2019 from top to bottom.

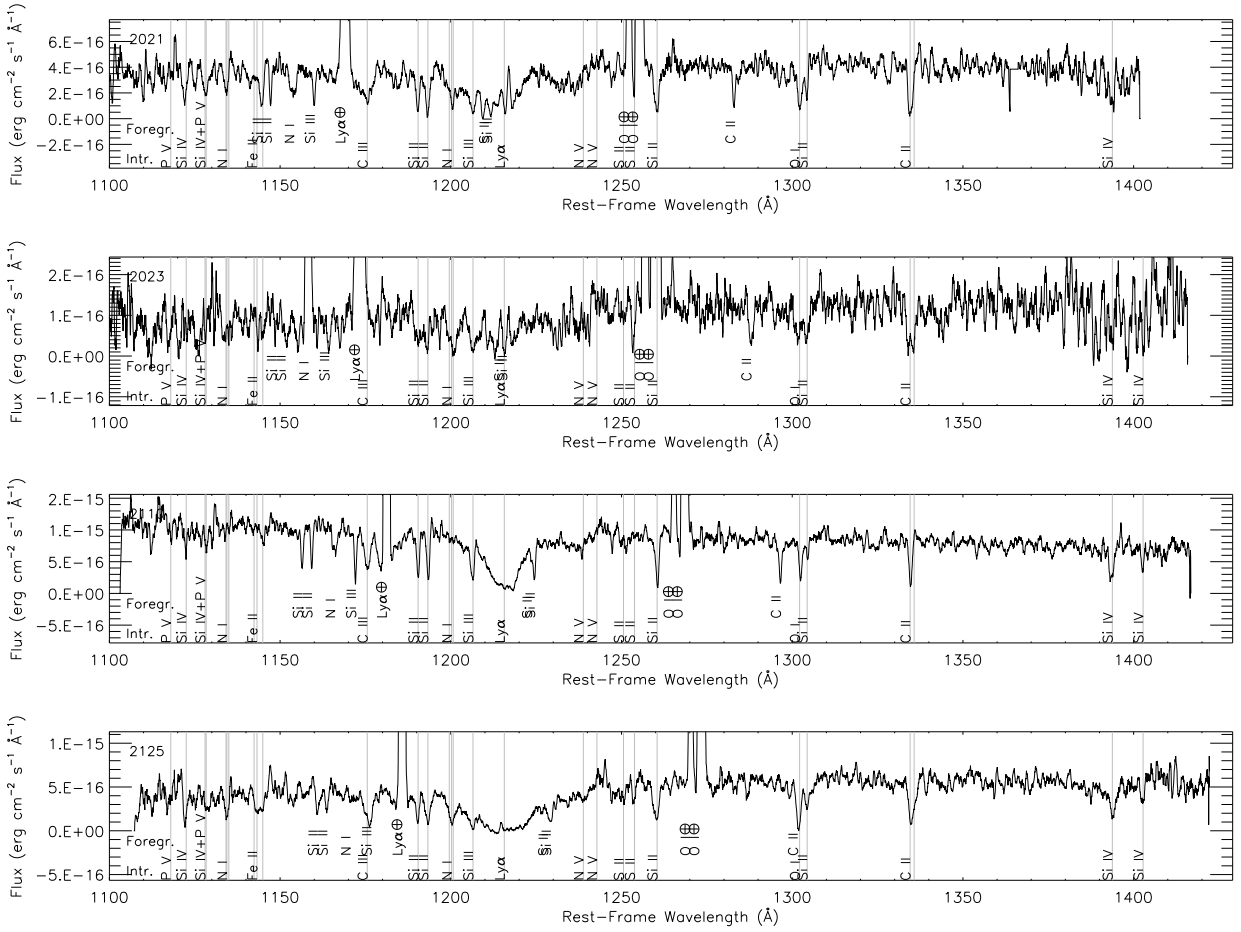


Fig. 8.— Similar to Figure 4 but for galaxies KISSR 2021, 2023, 2110, and 2125 from top to bottom.

Table 4. Wavelength Zero Point and Effective Spectral Resolution

Galaxy	$\langle v_{h,\oplus} \rangle$ km s ⁻¹	$\langle v_{h,MW} \rangle$ km s ⁻¹	$\langle \text{FWHM}_{MW} \rangle$ km s ⁻¹	$\langle \text{FWHM}_i \rangle$ km s ⁻¹
(1)	(2)	(3)	(4)	(5)
40	-32 ± 21	-78 ± 27	179 ± 91	287
108	-21 ± 5	-1 ± 5	109 ± 37	351
178	-27 ± 5	-62 ± 29	197 ± 24	332
182	-21 ± 13	-30 ± 12	132 ± 16	210
218	10	-26 ± 51	173 ± 45	391
242*	18 ± 5	-34 ± 8	110 ± 27	227
271*	-17 ± 5	-10 ± 43	74 ± 16	321
298*	15	-49 ± 17	75 ± 52	337
326*	-33	-90 ± 60	107	274
1084*	10 ± 2	-55 ± 9	185 ± 38	446
1567*	-17 ± 2
1578*	-11	-70 ± 4	125 ± 18	308
1637	2	-69 ± 71	305 ± 131	359
1785	-14 ± 2	-110 ± 4	142 ± 10	246
1942	-7 ± 21	-95 ± 61	179 ± 39	345
2019	-16 ± 6	-101 ± 13	188 ± 30	238
2021	-2 ± 4	-56 ± 25	174 ± 81	293
2023	-15 ± 9	-38 ± 72	198 ± 94	304
2110	-8 ± 15	-77 ± 9	138 ± 21	186
2125	-7 ± 14	-78 ± 14	274 ± 74	349
Min	-33	-110 ± 4	74 ± 16	186
Max	18 ± 5	-1 ± 5	305 ± 131	446

Note. — (1) KISSR ID of the galaxy. We mark the emitters with an asterisk. The last two rows give the minimum and maximum values in each column. In cases where more than one line was measured, we give the standard deviation of the various measurements, as the error. (2) & (3) Average heliocentric velocities, v_h , of geocoronal and MW lines, respectively. (4) & (5) Mean FWHM of MW and intrinsic ISM absorption lines. Values of < 110 km s⁻¹ in Column 5 are lower limits.

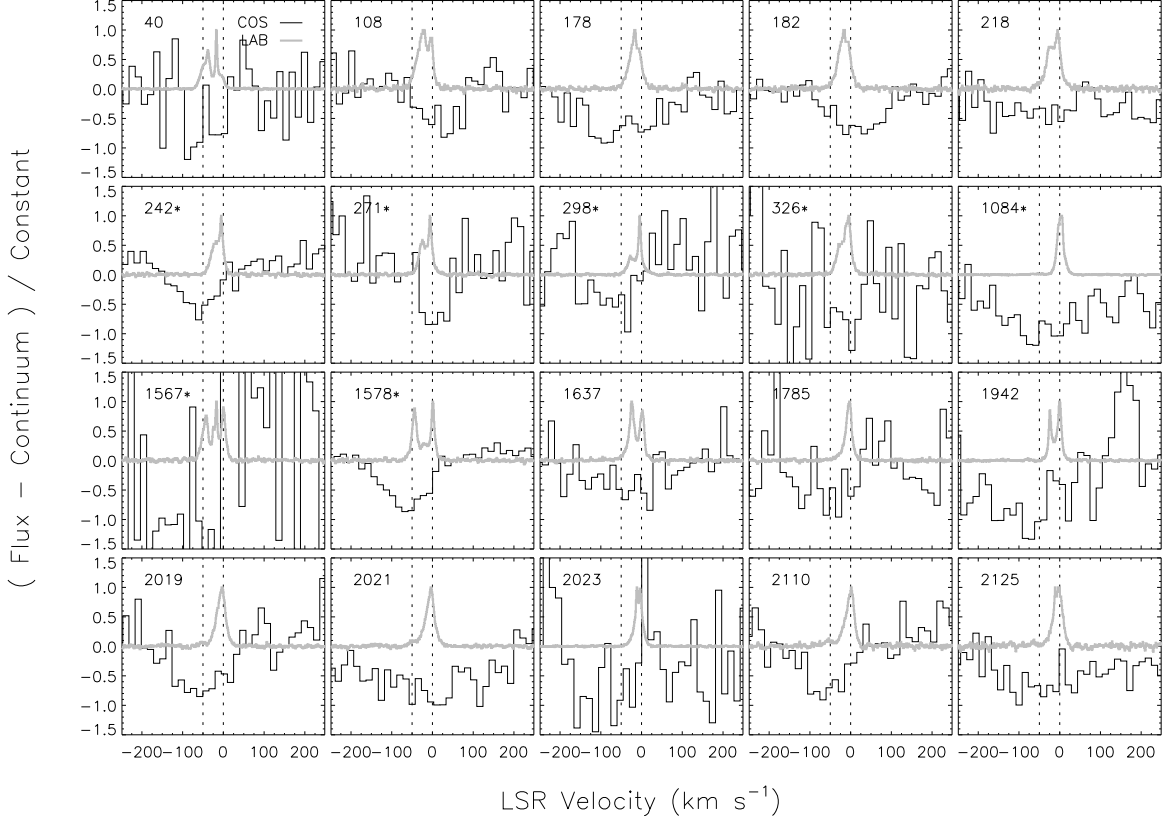


Fig. 9.— IVC H I 21 cm emission along the lines of sight to our targets (thick gray curves) and MW Si II $\lambda 1190$ absorptions (thin black curves). The spectral binnings are the nominal for the LAB and COS data, i.e., 1 km s^{-1} for the former and 16 km s^{-1} for the latter. We give the KISSR ID on the upper left of each panel. The seven galaxies with net Ly α in emission are marked with asterisks. The x-axis gives the velocity in the local standard of rest. The y-axis gives the continuum subtracted flux divided by a constant. The two vertical dotted lines correspond to $v_{\text{LSR}} = 0$ and 50 km s^{-1} .

redshifted to a mean velocity of $\langle v(\text{Ly}\alpha) \rangle = 172 \pm 49 \text{ km s}^{-1}$. KISSR 298 is a face-on spiral with two $\text{Ly}\alpha$ peaks separated by 370 km s^{-1} , such that one peak is redshifted and the other is blueshifted and twice as strong. The absorbers have $\text{Ly}\alpha$ troughs centered at a mean velocity of $\langle v(\text{Ly}\alpha) \rangle = 0 \pm 38 \text{ km s}^{-1}$. The $\text{Ly}\alpha$ mean velocities exclude KISSR 2021 and 2023 due to their noisy $\text{Ly}\alpha$ profiles.

The COS spectra include the H I gas tracers O I $\lambda 1302$, Si II $\lambda 1190$, and C II $\lambda 1334$. They also include Si III $\lambda 1206$, which traces gas in a higher ionization stage. Figure 11 shows the profiles of the previous metal lines in cases where the lines are not severely blended with contaminating lines. We omit emitter KISSR 1567, because for this object the target acquisition failed and the only observable line is $\text{Ly}\alpha$. The figure shows that C II $\lambda 1334$ and C II $\lambda 1336$ are resolved in the highest signal to noise spectra, e.g., for KISSR 242 and 1578.

For the emitters, the mean blueshifts of O I $\lambda 1302$ and C II $\lambda 1334$ are $\langle v(\text{OI}) \rangle = -117 \pm 47 \text{ km s}^{-1}$ and $\langle v(\text{CII}) \rangle = -94 \pm 20 \text{ km s}^{-1}$, respectively. For the absorbers, the corresponding mean velocity offsets are $\langle v(\text{OI}) \rangle = -23 \pm 28 \text{ km s}^{-1}$ and $\langle v(\text{CII}) \rangle = -21 \pm 31$, which is almost consistent with a static medium. Note that for spiral KISSR 2023, whose $\text{Ly}\alpha$ profile is very noisy, O I $\lambda 1302$ has a large blueshift (-153 km s^{-1}), such that $\text{Ly}\alpha$ emission would be expected. As previously mentioned, there appears to be some $\text{Ly}\alpha$ emission in this galaxy which has poor signal to noise. Interestingly, the SDSS image of KISSR 2023 is very similar to that of double-peaked emitter KISSR 298.

Our kinematical results are shown in Table 5, which lists the KISSR ID (Column 1); the $\text{Ly}\alpha$ profile shape (Column 2); the centroid of the $\text{Ly}\alpha$ line (Column 3); the velocity offsets between $\text{H}\alpha$ and intrinsic interstellar absorption lines Si II $\lambda 1190$, Si II $\lambda 1193$, Si III $\lambda 1206$, O I $\lambda 1302$, Si II $\lambda 1304$, and C II $\lambda 1334$ (Columns 4-9); the mean velocity offsets and standard deviations excluding Si III $\lambda 1206$ (Columns 10 & 11); the difference between the velocity offset of Si III $\lambda 1206$ and the value in Column 10 (Column 12); and for the $\text{Ly}\alpha$ absorbers, the H I column density of the Voigt profile (Column 13).

In summary, excluding the double emitter KISSR 298, we find that: i) $\text{Ly}\alpha$ is in emission and redshifted when high velocity outflows corresponding to expansion velocities of $\sim 100 \text{ km s}^{-1}$ are present, ii) $\text{Ly}\alpha$ is in absorption and at a velocity close to that of $\text{H}\alpha$ when null or low velocity gas flows are present, and iii) the $\text{Ly}\alpha$ redshift is higher than the blueshift of the LIS lines by a factor of 1.5 – 2. These results are further discussed in section 4. In addition, in cases where the centroid of Si III $\lambda 1206$ was measured, we find that this line tends to have a blueshift larger than that of the LIS lines by about $30 - 50 \text{ km s}^{-1}$.

3.3. $EW(\text{Ly}\alpha)$, $\text{Ly}\alpha$ escape fraction, and L_{1500}

In order to characterize the strength of $\text{Ly}\alpha$, we computed the $\text{Ly}\alpha$ luminosity $L(\text{Ly}\alpha)$, equivalent width, and escape fraction within the COS aperture. Although the relevant quantity for cosmological studies is the global integrated escape fraction of the galaxy, our measurements are

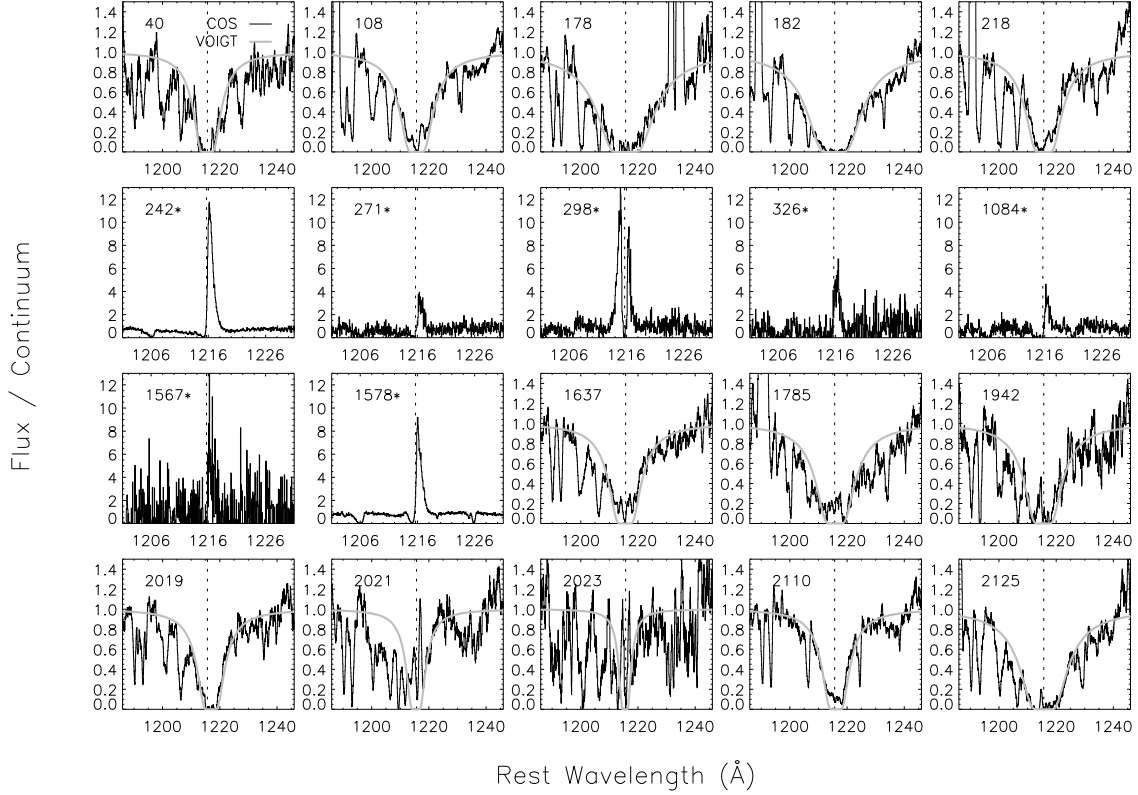


Fig. 10.— Intrinsic Ly α profiles of the galaxies corrected for redshift. We give the KISSR ID on the upper left of each panel. The seven galaxies with net Ly α in emission are marked with asterisks. The spectra are binned to 16 km s $^{-1}$. In addition, the spectra of the absorbers are smoothed for clarity. We overlay the Voigt profiles used for determining the Ly α absorption centroids (gray curves). The vertical dotted lines mark the rest-frame positions of Ly α . Note the double Ly α emission and stronger blue peak in KISSR 298. Also note that the Ly α profiles of KISSR 2021 and KISSR 2023 are rather noisy.

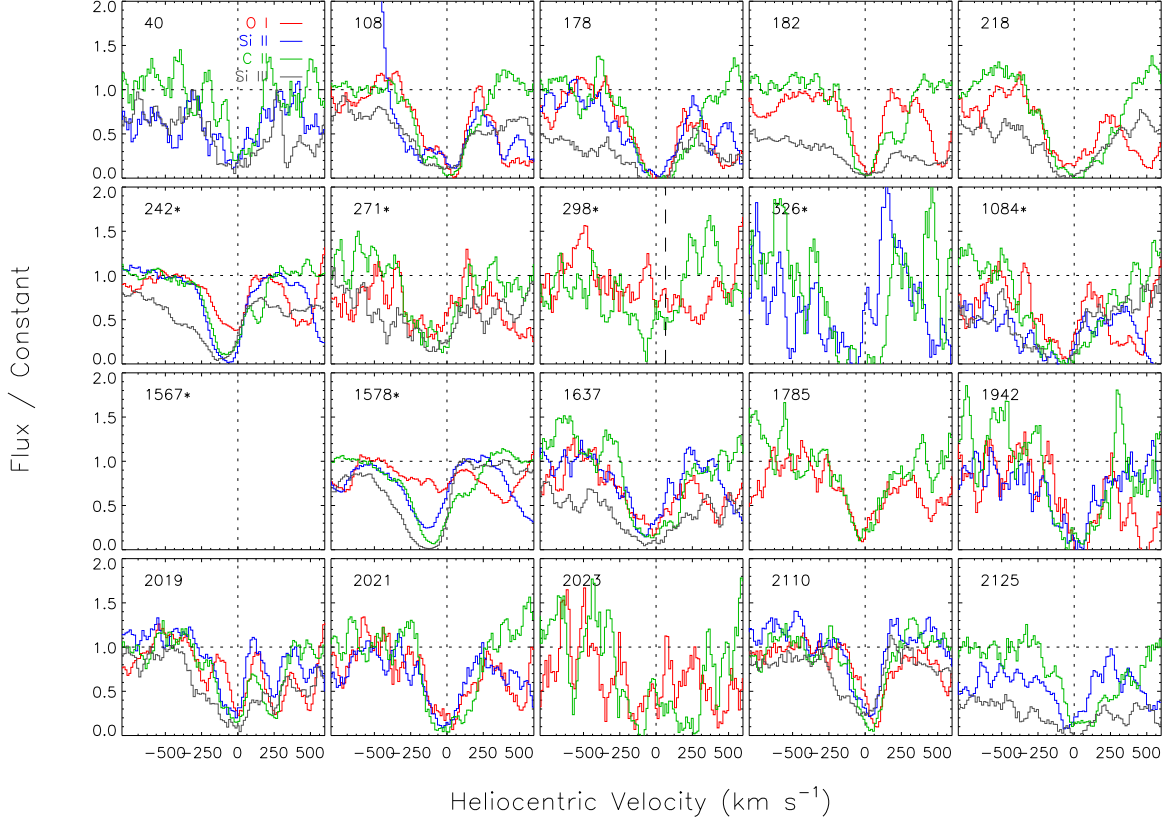


Fig. 11.— Velocity offsets between metal absorption lines intrinsic to the galaxies and $H\alpha$. We include $O\text{I } \lambda 1302$ (red), $\text{Si II } \lambda 1190$ (blue), $\text{C II } \lambda 1334$ (green), and/or $\text{Si III } \lambda 1206$ (gray), except when they are blended with contaminating lines. We give the KISSR ID on the upper left of each panel. The emitters are marked with asterisks. The spectra are binned to 16 km s^{-1} and smoothed for clarity. The vertical dotted lines mark a velocity offset of zero. For KISSR 298, which is a double-peaked $\text{Ly}\alpha$ emitter, we mark the position of the point equidistant from the two $\text{Ly}\alpha$ peaks with a vertical dashed line.

Table 5. ISM Kinematics

Galaxy	Ly α shape	Ly α 1216 km s $^{-1}$	Si II 1190 km s $^{-1}$	Si II 1193 km s $^{-1}$	Si III 1206 km s $^{-1}$	O I 1302 km s $^{-1}$	Si II 1304 km s $^{-1}$	C II 1334 km s $^{-1}$	$\langle\Delta v\rangle$ km s $^{-1}$	$\sigma(\Delta v)$ km s $^{-1}$	1206- $\langle\Delta v\rangle$ km s $^{-1}$	N(H I) cm $^{-2}$
(1)	(2)	(3)	(4)	(5)	(6)	(7)	(8)	(9)	(10)	(11)	(12)	(13)
40	Ab	-22	-29	-29	-29	0	...	5.0E+20
108	Ab	0	-57	-96	-48	...	-50	-52	5	44	7.5E+20
178	Ab	2	-35	-48	-17	-33	16	...	2.3E+21
182	Ab	-37	-46	-47	-34	-33	-47	-40	8	7	2.0E+21
218	Ab	10	-32	-11	23	-7	28	...	9.0E+20
242	P-Cygni	170 \pm 46	-68	-73	-130	-53	-104	-79	-76	19	55	...
271	P-Cygni	152 \pm 20	-177	...	-113	-145	45
298	2 Em	-118 \pm 11, 249 \pm 17	-185	-162	-192	-100	-151	47	33	...
326	P-Cygni	251 \pm 24	-162	-140	...	-83	-175	-88	-130	42
1084	P-Cygni	198 \pm 20	-169	-86	-146	-109	-125	-78	-113	36	33	...
1567	P-Cygni	105 \pm 41
1578	P-Cygni	158 \pm 2	-163	-147	-166	-116	-149	-127	-140	19	26	...
1637	Ab	-50 ...	-68	-65	-60	-54	-69	-9	-53	25	6	7.0E+20
1785	Ab	50	-24	-61	-42	-42	19	...	1.0E+21
1942	Ab	-50 ...	-7	-2	...	6	-63	-24	-18	27	...	9.5E+20
2019	Ab	50 ...	-54	-64	-37	-25	...	-59	-50	18	-14	3.5E+20
2021	Ab	-50	-38	-28	-19	-8	-18	-14	-21	12	-2	2.5E+20
2023	Ab	-50	-153	-62	-171	-128	58	...	1.0E+20
2110	Ab	50 ...	-13	6	-76	36	15	-2	8	19	85	3.5E+20
2125	Ab	0	-56	-38	-44	48	-22	48	...	1.5E+21

Note. — (1) KISSR ID. (2) Profile shape of Ly α . Ab=absorption. P-Cygni=P-Cygni like. 2 Em=Two emission peaks. (3) Velocity offset between the centroid of the Ly α line and H α . (4)-(9) Velocity offset between the centroid of the intrinsic metal absorption line and H α . (10) Mean velocity offset of intrinsic metal lines excluding Si III λ 1206. (11) Standard deviation of the velocities of the intrinsic metal lines excluding Si III λ 1206. (12) Velocity offset between Si III λ 1206 and the mean of the lower ionization intrinsic metal lines. (13) H I column density derived from Voigt profiles.

useful for comparing with global values derived from Ly α line images, as they give an idea of the concentration of the emission and of how coincident it is with regions of high FUV surface brightness. Such Ly α maps have been or will be obtained for a portion of our targets. We computed two values of the escape fraction, one using H α and the other using H β . Both adopt the case B recombination theory predictions of Osterbrock & Ferland (2006) for $T_e \sim 10^4$ K and $n_e = 10^2$ cm $^{-3}$, i.e., Ly α /H α =8.1 and Ly α /H β =23.1. $L(\text{Ly}\alpha)$. The escape fractions were computed before and after correcting for the dust attenuation. We also computed the COS luminosity of the continuum at 1500 Å, L_{1500} , for comparison with the value from *GALEX*, which is given in Table 1. In order to obtain L_{1500} , we extrapolated beyond the red edge of our data which is less than 1500 Å. In this paper, L_{1500} is used for deriving the mass of the dominant stellar population and the star formation rate (see below).

For correcting the hydrogen line fluxes and L_{1500} for the dust attenuation, we derived the total color excess, $E(B - V)_t$, from the observed H α /H β line intensity ratio, after correcting the Balmer lines for the underlying stellar absorption. The stellar absorption correction was done by adding 2 Å to the equivalent widths of the Balmer lines, following (McCall et al. 1985). This increases the H α flux by 2% and the H β flux by 13% (median values for the sample). We did not correct the interstellar Ly α for the stellar contribution at Ly α , since as mentioned in the introduction, this correction is expected to be small for stellar populations dominated by O and early B stars, as is the case for the Ly α emitters in our sample. That O and early B stars dominate for the emitters is shown in section 3.5. The Ly α emission line fluxes were obtained by numerical integration. The Balmer line fluxes were obtained from the SDSS data when available and from the KISS data otherwise. The SDSS spectra have higher spectral resolution.

The total color excess is given by $E(B - V)_t = E(B - V)_G + E(B - V)_i$, where $E(B - V)_G$ and $E(B - V)_i$ are the Galactic and intrinsic contributions, respectively. According to the Milky Way reddening maps of Schlegel et al. (1998), $E(B - V)_G$ is small towards our targets (see Table 1), thus most of the extinction must be intrinsic. Since Valls-Gabaud (1993) and Calzetti & Kinney (1992) showed that by using a metallicity-dependent reddening law one could recover the theoretical Ly α /H β ratio, we tried using a MW law for the spiral galaxies and an SMC law for the irregular galaxies. For this purpose, we used the reddening laws tabulated in Osterbrock & Ferland (2006). However, we found that the $E(B - V)_t$ values derived from these two laws are very similar. In the end, and as in Calzetti et al. (2000), we adopted a MW law for deriving $E(B - V)_t$. For the theoretical H α /H β ratio we used 2.86, which is the case B recombination theory prediction for $T_e = 10^4$ K and $n_e = 100$ cm s $^{-3}$ of Osterbrock & Ferland (2006).

In order to see if the relation $E(B - V)_s = 0.44 \times E(B - V)_t$ of Calzetti et al. (2000) holds for our data, we computed the color excess of the stellar continuum, $E(B - V)_s$, using the slope of the FUV continuum, β . For obtaining $E(B - V)_s$ we used the method outlined in Wofford et al. (2011), where the slope of the Milky-Way de-reddened continuum is compared to that of a dust-free model of the appropriate metallicity. Following Calzetti et al. (2000), $E(B - V)_s$ was derived using the starburst reddening law. The comparison was done over the wavelength range from 1200 Å to

the red edge of the data. The red edge is redshift-dependent, as shown in Figures 4-8, and it is always less than 1500 Å. This range is different from what is used in Calzetti et al. (2000), i.e., 1250 – 1950 Å.

Our results are shown in Table 6, which gives the KISSR ID of the galaxy (Column 1); the rest-frame value of $EW(\text{Ly}\alpha)$ (Column 2); $L(\text{Ly}\alpha)$, L_{1500} from the COS spectra, $L(\text{H}\alpha)$, and $L(\text{H}\beta)$ (Columns 3-6, uncorrected for dust extinction); the escape fractions within the COS aperture, i.e. $\text{Ly}\alpha/\text{H}\alpha/8.1\times 100$ and $\text{Ly}\alpha/\text{H}\beta/23.1\times 100$ (Columns 7 & 8); $E(B - V)_t$ from the Balmer lines and $E(B - V)_s$ from the slope of the FUV continuum (Columns 9 & 10); and the reddening-corrected values of L_{1500} , $\text{H}\alpha/\text{H}\beta$, and the escape fractions (Columns 11-14).

In summary, we find that $E(B - V)_s = 1.27 \times E(B - V)_t$ (adopting the median of the sample), i.e., that the stellar continuum is more reddened than the nebular continuum, contrary to what was found by Calzetti et al. (2000). The different result is attributed to the larger optical and ultraviolet apertures used by Calzetti et al. (2000), and to the different wavelength range used by the latter authors for fitting the UV continuum. We also find that the rest-frame EW s of the emitters are in the range 1 – 12 Å, and that the reddening corrected escape fractions of the emitters are in the range 1 – 12%. The latter two results are further discussed in section 4. Finally, we found that L_{1500} from the COS data is lower by a factor of a few compared to the value from *GALEX* (compare column 4 of Table 6 with column 9 of Table 1). This is attributed to the larger aperture of *GALEX*.

3.4. SED Models

We studied how the strength of $\text{Ly}\alpha$ relates to the starburst phase and star formation rate of the dominant stellar population by comparing the COS observations with synthetic dust-free spectra computed with the widely used package Starburst99 (S99, Leitherer et al. 1999, 2010; Vázquez & Leitherer 2005). The observed star formation rate is that within the COS aperture. The value of $EW(\text{Ly}\alpha)$ depends on the metallicity, IMF, star formation history, and evolutionary phase of the stellar population (see models by Valls-Gabaud 1993; Charlot & Fall 1993; Verhamme et al. 2008). Because empirical spectral stellar libraries in the UV are only available at the Galactic ($Z_{\odot} = 0.013$, Asplund et al. 2009) and LMC/SMC ($Z_{\text{LMC}} = 0.007$ and $Z_{\text{SMC}} = 0.002$, Maeder et al. 1999) metallicities, we have to rely on theoretical libraries at other metallicities. We used the theoretical libraries of Leitherer et al. (2010) corresponding to $Z = 0.001, 0.004, 0.008, 0.020$, and 0.040 . For comparison, we also computed models with the empirical Galactic and LMC/SMC stellar libraries. We will refer to simulations based on the theoretical and empirical libraries as the theoretical and empirical models, respectively. The theoretical models use stellar evolution tracks corresponding to $Z = 0.020$ and model atmospheres corresponding to $Z = Z_{\odot}$. The empirical models use tracks corresponding to $Z = 0.020$ or $Z = 0.004$. Our grid of models includes single stellar population (SSP) and continuous star formation (CSF) scenarios. Continuous star formation is more appropriate in our case, as the observed spectra include light from regions of a few kpc in size

Table 6. Ly α Escape Fractions

Galaxy	EW(Ly α) Å	logL(Ly α) erg s $^{-1}$ uncorr	logL $_{1500}$ erg s $^{-1}$ uncorr	logL(H α) erg s $^{-1}$ uncorr	logL(H β) erg s $^{-1}$ uncorr	f(H α) % uncorr	f(H β) % uncorr	E(B-V) $_t$ mag Balmer	E(B-V) $_s$ mag β	logL $_{1500}$ erg s $^{-1}$ corr	H α /H β	f(H α) % corr	f(H β) % corr
(1)	(2)	(3)	(4)	(5)	(6)	(7)	(8)	(9)	(10)	(11)	(12)	(13)	(14)
40	< 0	...	38.6	40.02	39.54	0.04	0.21	39.5	3.1
108	< 0	...	39.1	40.38	39.85	0.15	0.17	39.9	3.5
178	< 0	...	39.6	41.21	40.64	0.23	0.20	40.5	4
182	< 0	...	39.1	40.41	39.88	0.16	0.19	39.9	3.6
218	< 0	...	38.9	40.49	39.87	0.33	0.41	40.6	4.6
242*	10	41.20	40.1	41.61	41.07	5	6	0.18	0.21	41.0	3.7	12	14
271*	1	38.74	38.5	0.17	0.28	39.7
298*	12	40.16	39.3	40.65	40.06	6	2	0.28	0.39	41.0	4.3	12	15
326*	4	39.30	38.7	40.22	39.61	2	0	0.16	0.38	40.3	4.4	7	9
1084*	1	38.99	39.0	41.03	40.37	0	1	0.42	0.44	41.0	5.2	1	1
1567*	3	38.71	38.3	40.25	39.63	0	1	0.15	0.31	39.6	4.7	2	3
1578*	7	41.00	40.0	41.55	41.04	3	4	0.12	0.10	40.4	3.4	6	7
1637	< 0	...	39.2	40.43	39.93	0.10	0.30	40.5	3.3
1785	< 0	...	38.5	40.38	39.83	0.18	0.19	39.3	3.7
1942	< 0	...	38.9	40.00	39.44	0.21	0.28	40.1	3.9
2019	< 0	...	39.1	40.63	40.17	0.01	0.14	39.7	2.9
2021	< 0	...	39.2	40.59	40.03	0.21	0.30	40.5	3.8
2023	38.6	40.58	39.91	0.45	0.31	39.9	5.5
2110	< 0	...	39.1	40.33	39.86	0.00	0.09	39.5	3
2125	< 0	...	38.9	40.73	40.03	0.49	0.30	40.2	5.7
Min	1	38.71	38.3	40.00	39.44	0	0	0.00	0.09	39.3	2.9	1	1
Max	12	41.20	40.1	41.61	41.07	6	6	0.49	0.44	41.0	5.72	12	15

and such large regions must contain UV-bright star clusters that span a range of ages. The SSP models are for comparison. We adopted a Kroupa IMF (Kroupa 2001), as at the high-mass end, it is considered to be universally applicable (Bastian et al. 2010). We used the Geneva stellar evolution tracks for non-rotating single-stars with high-mass loss (Schaller et al. 1992; Meynet et al. 1994) because models that account for stellar rotation and binarity (Eldridge et al. 2008; Levesque et al. 2012) are still under development and require calibration against observations over our range of metallicities. Finally, we did not compute models for times earlier than 2 Myr because this is the age of the youngest LMC main-sequence O stars, or greater than 30 Myr after the beginning of star formation since the SSP models are affected by incompleteness of the stellar libraries beyond this time and the continuum slope and age-sensitive stellar-wind lines of CSF models do not significantly change beyond this time.

3.5. Starburst Phase, Stellar Mass, and Star Formation Rate

The age of an FUV-bright stellar population can be derived spectroscopically by comparing the observed profiles of age sensitive lines originating in the winds of massive stars with model spectra. The strong N v λ 1238.8, 1242.8, Si iv λ 1393.8, 1402.8, and C iv λ 1548.2, 1550.8 resonant doublets are widely used for this purpose (Tremonti et al. 2001; Chandar et al. 2003; Wofford et al. 2011). In summary, the P-Cygni profiles of the N v and the C iv doublets decrease in strength as the O stars evolve and expire. On the other hand, the Si iv doublet develops a P-Cygni profile in giant and supergiant O stars. Unfortunately, the C iv doublet and sometimes the Si iv doublet fall outside of the wavelength range that we observed with COS. In addition, the N v doublet is sometimes contaminated with geocoronal emission. However, for targets showing clean and strong N v P-Cygni profiles, the age of the dominant population is younger than ~ 10 Myr (see figure 5 in Wofford et al. 2011). Furthermore, a large H α equivalent also indicates the presence of a young population (Kennicutt 1998; Leitherer et al. 1999).

We compared the COS spectra with SSP and CSF models of 5 and 10 Myr. We select this age range because between 5 and 10 Myr, the strength of N v noticeably decreases and these ages are sufficient for our purpose of demonstrating how young the dominant stellar populations are. We found the best-fit model to the N v and Si iv profiles by eye. The comparison was performed on the rectified spectra, as the models are dust-free but the data are not. The metallicity of the model is that most appropriate for the galaxy based on its oxygen abundance⁴. Figures 12 and 13 show the comparisons of the observed N v and Si iv profiles with the theoretical models. Similarly, Figures 14 and 15 show the comparisons with the empirical models.

A comparison of the theoretical and empirical models in Figures 12 and 14 shows that at both

⁴We adopted stellar evolution tracks with a metallicity $\log_{10}(Z/Z_{\odot}) \sim \log_{10}[(O/H)/(O/H)_{\odot}]$, where $Z_{\odot} = 0.020$ corresponds to $12 + \log_{10}(O/H)_{\odot} = 8.83$, i.e., to the old solar value of Grevesse & Sauval (1998).

ages and at all metallicities, N v is stronger for the CSF models than for the SSP models, although the difference is less at the lowest metallicity (e.g., for 2019 and 2110). Furthermore, the theoretical CSF models yield stronger N v profiles than the empirical models at similar ages and metallicities (e.g., 40 and 242). Conversely, the theoretical Si iv profiles show weaker emission components than the empirical ones. These differences do not severely affect our results.

The observed N v profiles of Ly α emitters 298, 326, and 1567 are contaminated with geocoronal O I lines, and the Si iv profiles of 11 targets, including four of the seven emitters, are either incomplete or have low signal to noise. For this reason, and because the Si iv profiles from the theoretical models are too weak compared to observations at young ages (e.g., compared to the empirical models), in the rest of our age-dating analysis, we concentrate on the N v profiles. For targets with clean N v profiles, we find that the theoretical SSP models tend to be a better fit than the theoretical CSF models, except at the lowest metallicity (e.g., KISSR 2019 and 2110), where the SSP and CSF N v profiles are very similar. This is true for the Ly α emitters as well as for the Ly α absorbers. One exception is 1084, which is better fitted by a CSF model. In any case, Ly α absorbers such as spiral galaxy KISSR 218 and metal-poor galaxies KISSR 2019 and 2110 have strong N v profiles and large H α *EW*s indicative of ages younger than ~ 10 Myr. Thus, they would be expected to have strong Ly α emission. However, they are absorbers, which is consistent with their low gas-flow velocities (see Table 5). In addition, one cannot rule out attenuation of Ly α due to the presence of dust. We also find that the emitters have Ly α equivalent widths that are consistent with their young ages, but that are small compared to model predictions for young starbursts. Thus, the emitters also require the presence of scattering in H I and attenuation by dust. The take away point is that even at young ages ($\lesssim 10$ Myr) targets can show Ly α in absorption if the gas surrounding the starburst is almost static or if the dust column density surrounding the hot stars is significant.

Table 7 gives the stellar masses and star formation rates derived from the UV spectra by adopting the ages in the second column of the table. For a given age, metallicity, IMF, and star formation history, the theoretical value of L_{1500} only depends of the mass of the stellar population. We give two estimates of the mass and the star formation rate, one corresponding to the SSP and the other to the CSF model. The masses are derived from the comparison of the observed and computed luminosities of the stellar continuum at 1500 Å (both dust-free). For the computed luminosity, we use the mean of the theoretical and empirical predictions at the adopted age and metallicity. Note that for the SSP models, it is common practice to define a characteristic star formation rate as the ratio of the stellar mass to the age of the population. This is what we quote in column 5 of Table 7. For comparison, the table also gives the star formation rate derived from the SDSS H α luminosity (corrected for reddening using the starburst attenuation law of Calzetti et al. (2000)) and equation (2) in Kennicutt (1998). We recall that the SDSS aperture is very similar to the COS aperture. This is not the case for the KISS data, therefore, we omit the optical SFR for targets without SDSS data. We also recall that the star formation rates are not global values. We find that the SSP models yield higher masses and star formation rates than the CSF models

by a factor of 1.4 (median). This is because CSF models predict larger values of L_{1500} than the SSP models at the adopted ages. We also find that the SSP models yield systematically higher star formation rates than those derived using $H\alpha$ by a factor of 5 (median) with a standard deviation of 7. The UV SSP SFRs derived from L_{1500} should be viewed with caution as they are inversely proportional to the ages, which are expected to be underestimated by a factor of a few in cases where $N\text{V}$ is contaminated with geocoronal emission or does not show a strong P-Cygni profile. This is the case for KISSR 298 and 1637, which show the largest disagreement between the optical and the UV SFRs. In addition, the UV SSP SFRs depend on the masses, and Wofford et al. (2011) found systematically higher masses derived from L_{1500} compared to masses derived from optical photometry for individual star clusters. On the other hand, in some cases, the agreement between the optical and UV SFRs is very good. This is the case for KISSR 1578, a target with a prominent $N\text{V}$ doublet and a high S/N spectrum. Unfortunately, only four emitters have $H\alpha$ SFRs, which makes it difficult to study trends between $\text{Ly}\alpha$ and the SFR.

3.6. Wolf-Rayet Stars

The detection of broad (FWHM $\sim 10 \text{ \AA}$, Conti 1991) $\text{He II } \lambda 4686$ emission (hereafter, He II emission) provides another way of estimating the age of a stellar population. In the absence of an AGN, such emission originates in the dense winds of WR stars (Beals 1929; Bibby & Crowther 2012), whose progenitors are massive stars ($M_{\text{initial}} \gtrsim 25$, Maeder & Meynet 1994) with lifetimes of ~ 5 Myr (Meynet & Maeder 2005). Other optical WR emission lines are $\text{C III } \lambda 4650$ and $\text{N III } \lambda 4640$, which are generally weaker. For each galaxy, we show in Figure 16 the spectral region around the $\text{He II } \lambda 4686$ line. The figure shows that in some cases, the $[\text{Fe III}] \lambda 4658$ peak is taller than the $\text{He II } \lambda 4686$ peak. As in López-Sánchez & Esteban (2010), we used multiple Gaussians to fit the spectral region in the vicinity of 4686 \AA . The Gaussian centers were fixed at wavelengths where lines were expected. We detect He II at the 3σ level or better in six cases, i.e., the amplitude of He II is at least three times the standard deviation of the nearby continuum in six cases. In five of the latter cases, the He II line is broad, i.e., FWHM $\sim 10 \text{ \AA}$. Unfortunately, for four of the seven $\text{Ly}\alpha$ emitters, the optical spectrum is either unavailable (KISSR 271), of inadequate spectral resolution (KISSR 326 and KISSR 1567), or very noisy (KISSR 298). The three emitters with adequate optical spectra have He II detections with FWHM $\geq 6 \text{ \AA}$. This includes KISSR 1084, which may be of composite spectral type, and whose broad He II emission is accompanied by narrow/nebular He II emission. Note that for the latter galaxy, the He II peak is taller than the $[\text{Fe III}] \lambda 4658$ peak, unlike in most galaxies with broad He II emission. On the other hand, two of the non- $\text{Ly}\alpha$ emitters have He II detections and FWHM $\geq 7 \text{ \AA}$. The lack of $\text{Ly}\alpha$ emission in galaxies with broad He II emission could be due to the lack of significant gas flow in the direction towards the observer. This is the case of KISSR 178 and the highly inclined spiral KISSR 2125. Finally, the non-emitter KISSR 108 only shows narrow He II emission. Shirazi & Brinchmann (2012) interpret the presence of narrow He II emission without a broad component, as WR stars that are offset from the emitting gas.

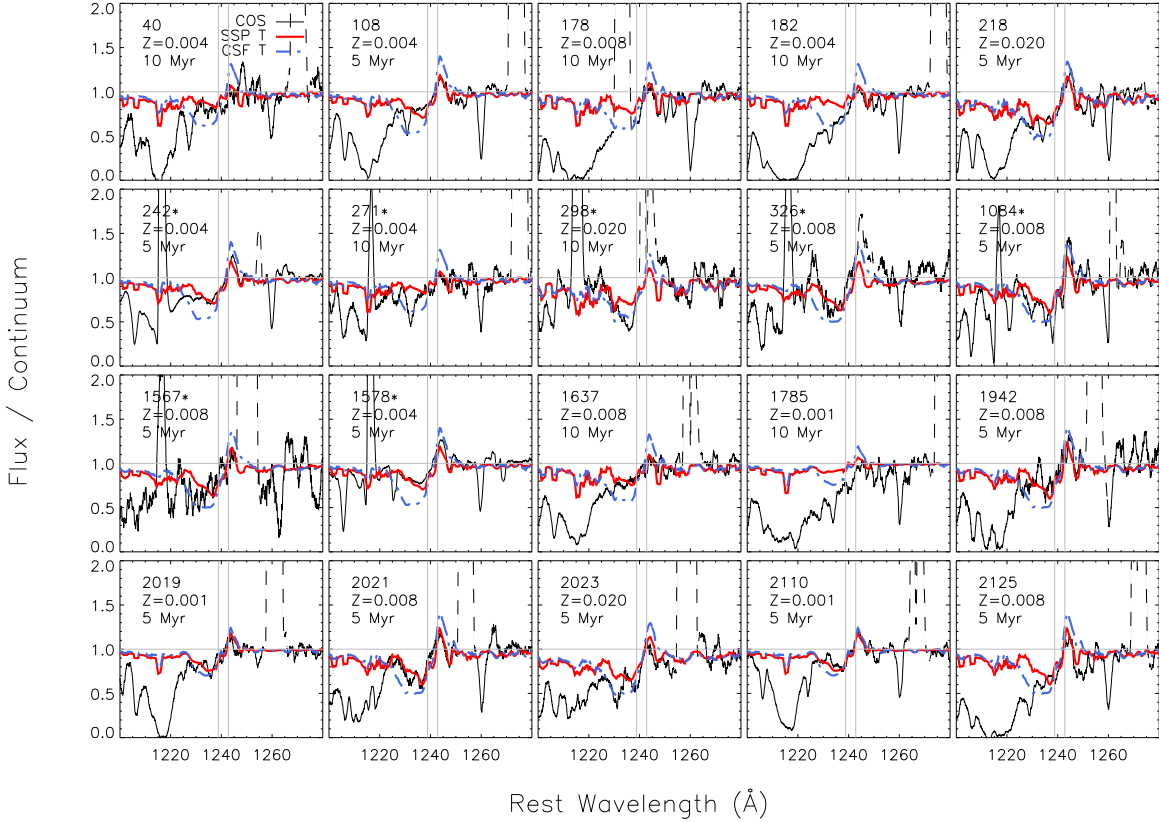


Fig. 12.— Comparison of observed and computed N v 1240 resonance doublets. The vertical gray lines give the rest wavelengths of the N v lines. The observations (thin black curves) are sometimes contaminated with geocoronal lines (dashed lines). We show SSP models (thick red curves) and CSF models (dotted-dashed blue curves) based on theoretical (T) stellar libraries. Such models only include stellar lines and are not optimized for the stellar Ly α . The models correspond to either 5 or 10 Myr, depending on which model fits better. In each panel, we give the KISSR ID, the model age, and the model metallicity. The Ly α emitters are marked with asterisks.

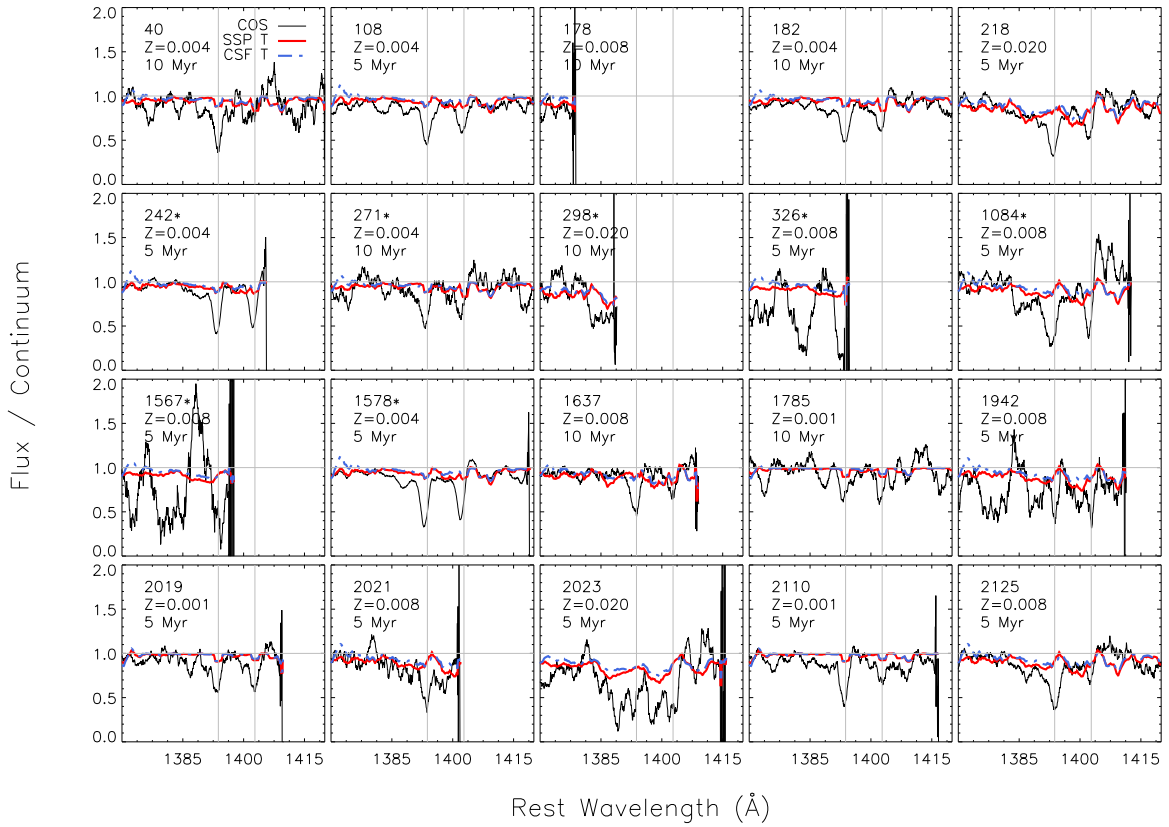


Fig. 13.— Similar to Figure 12 but for the Si IV 1400 resonance doublets. The vertical gray lines mark the positions of the Si IV lines.

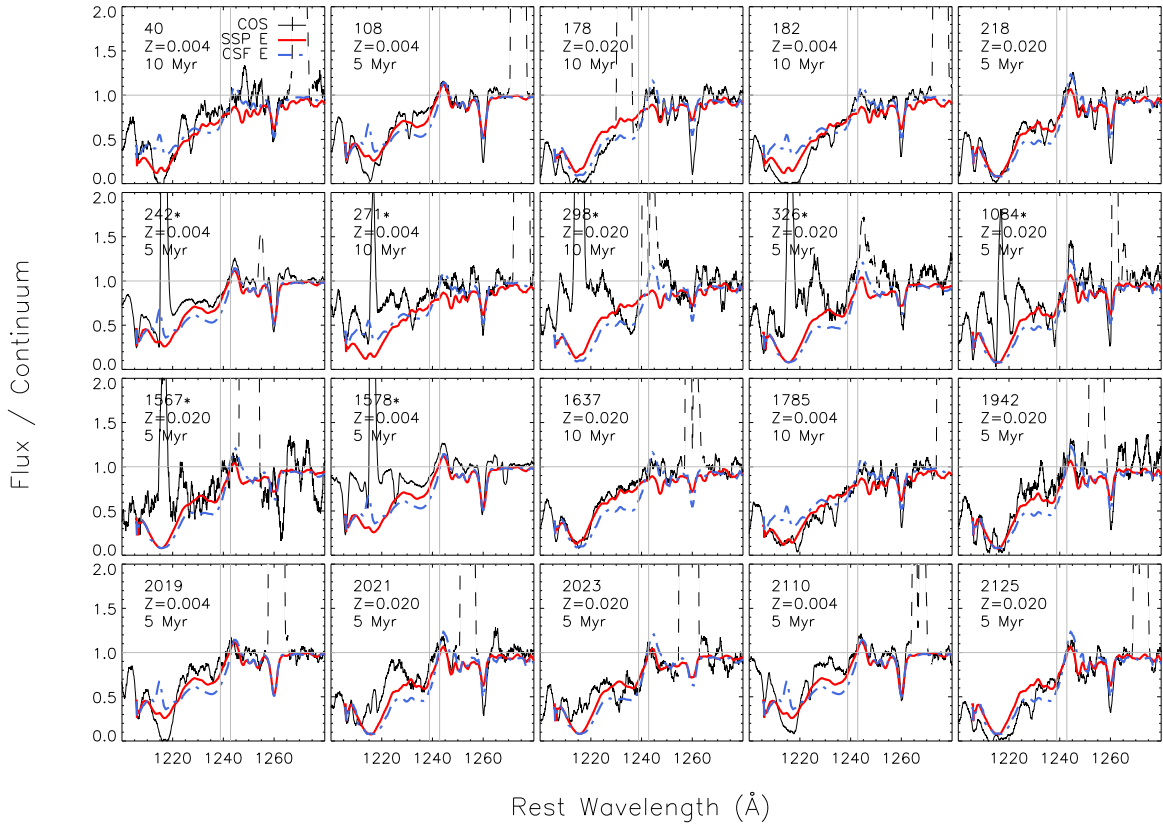


Fig. 14.— Similar to Figure 12 but the models are based on empirical (E) stellar libraries. The empirical models are contaminated with Milky Way lines, in particular, Ly α . Only two metallicities are available for the empirical models.

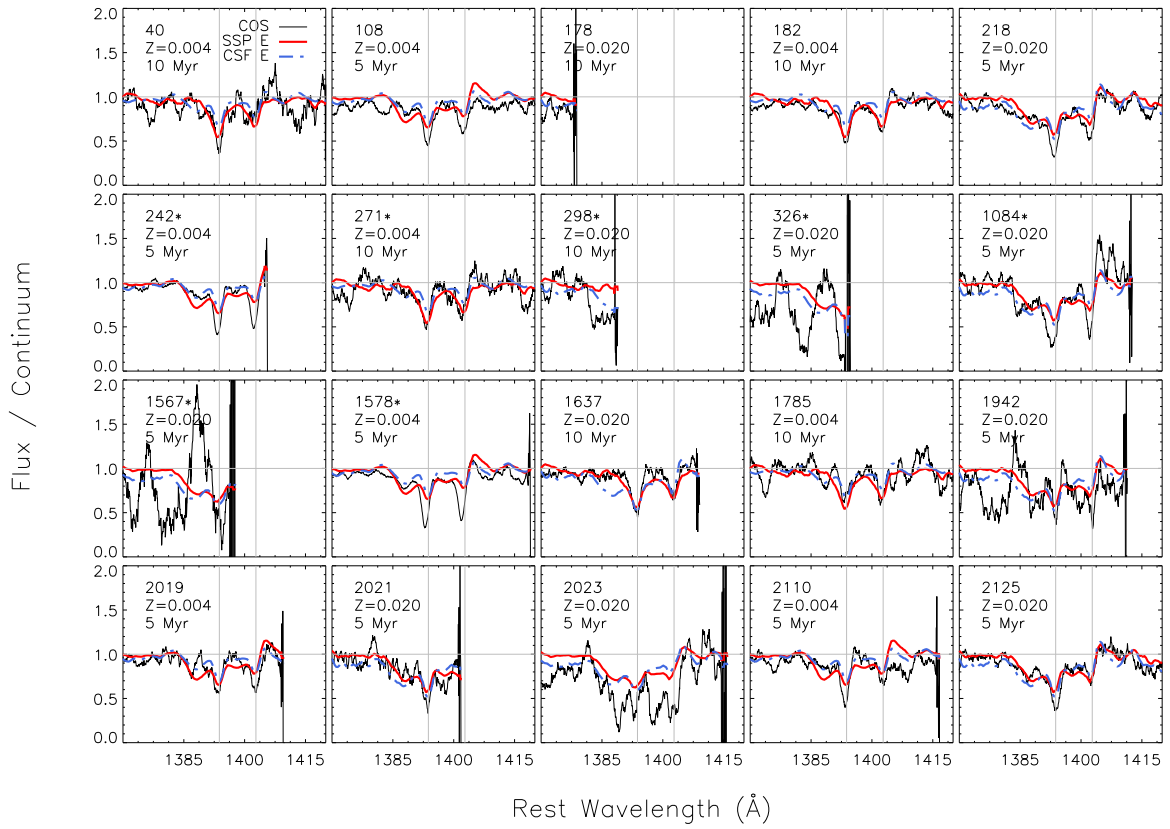


Fig. 15.— Similar to Figure 14 but for the Si IV 1400 resonance doublets.

Table 7. Stellar Population Properties

Galaxy	Age	Mass SSP	Mass CSF	SFR SSP	SFR CSF	SFR H α
	Myr	M $_{\odot}$	M $_{\odot}$	M $_{\odot}$ yr $^{-1}$	M $_{\odot}$ yr $^{-1}$	M $_{\odot}$ yr $^{-1}$
(1)	(2)	(3)	(4)	(5)	(6)	(7)
40	10	7E+06	3E+06	0.7	0.3	0.1
108	5	7E+06	5E+06	1.4	0.9	0.3
178	10	7E+07	3E+07	6.8	2.7	2.6
182	10	2E+07	6E+06	1.6	0.6	0.3
218	5	4E+07	2E+07	7.2	5.0	0.7
242*	5	9E+07	6E+07	17.6	12.1	5.6
271*	10	1E+07	5E+06	1.1	0.5	...
298*	10	2E+08	8E+07	19.7	7.9	0.8
326*	5	2E+07	1E+07	3.8	2.6	...
1084*	5	9E+07	6E+07	18.5	12.8	3.1
1567*	5	4E+06	3E+06	0.8	0.5	...
1578*	5	3E+07	2E+07	5.0	3.5	4.0
1637	10	6E+07	3E+07	6.5	2.6	0.3
1785	10	5E+06	2E+06	0.5	0.2	0.3
1942	5	1E+07	8E+06	2.3	1.6	0.2
2019	5	5E+06	3E+06	1.0	0.7	0.3
2021	5	3E+07	2E+07	5.2	3.6	0.6
2023	5	7E+06	5E+06	1.5	1.0	1.2
2110	5	3E+06	2E+06	0.6	0.4	...
2125	5	1E+07	1E+07	2.9	2.0	1.9
Min	-	3E+06	2E+06	0.5	0.2	0.1
Max	-	2E+08	8E+07	19.7	12.8	5.6
Mean	-	4E+07	2E+07	5.2	3.1	1.4
Sigma	-	5E+07	2E+07	6.2	3.7	1.6

Note. — (1) KISSR ID identifier. The emitters are marked with asterisks. (2) Adopted age. (3) to (6) Stellar population masses and star formation rates corresponding to the COS aperture and derived by comparing the observed and computed UV spectra. The computed spectra correspond to the adopted ages and to SSP or CSF models. (7) Star formation rate derived from the reddening-corrected H α luminosity. The last four rows give the minimum, maximum, mean, and standard deviation for each column.

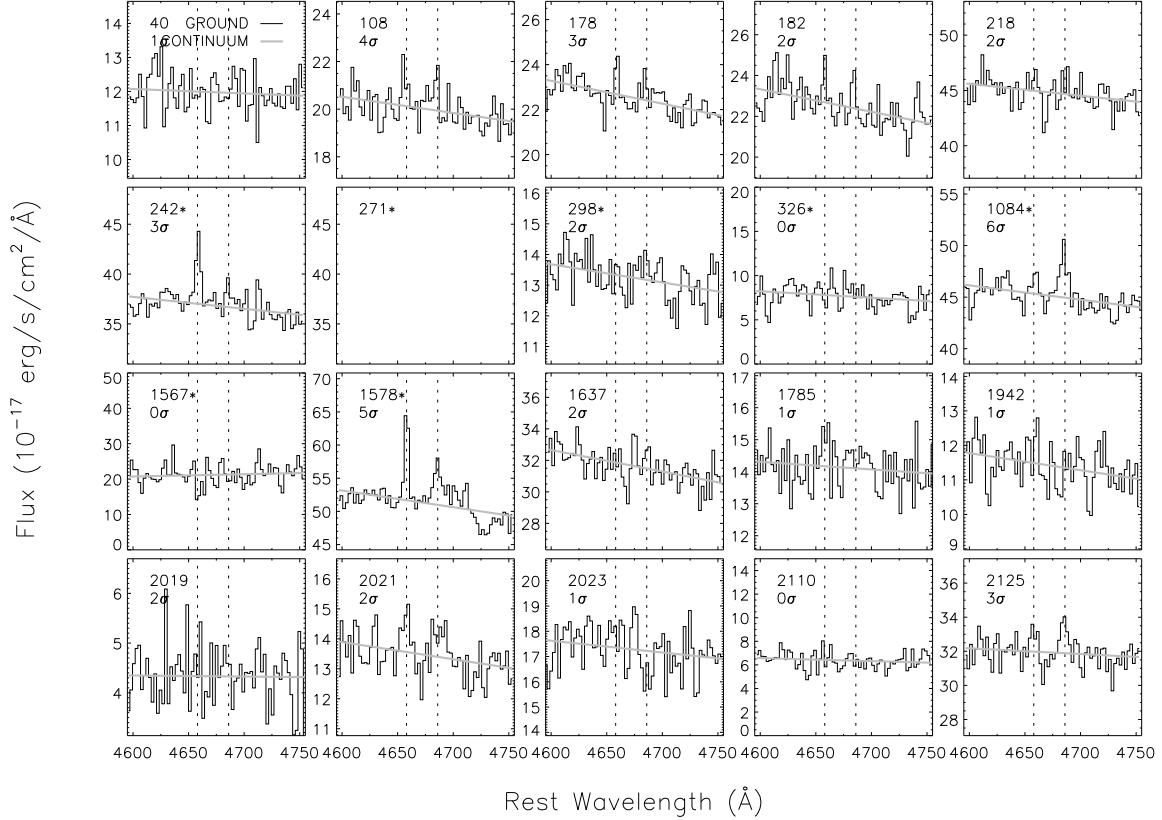


Fig. 16.— Spectral region around He II $\lambda 4686$. The legends give the KISSR ID and the ratios of the amplitude of He II to the standard deviation of the nearby continuum. The spectra are from the SDSS DR7 except for galaxies KISSR 326, 1567, and 2110 whose spectra are from Salzer et al. (2005). We do not have an optical spectrum for 271. We degraded the SDSS spectral resolution to match that of the non-SDSS spectra, which is 2.4 \AA . The spectra are corrected for redshift and uncorrected for reddening. The dashed vertical lines mark the positions of the $[\text{Fe III}] \lambda 4658$ and He II $\lambda 4686$ emission lines. We overlay in gray a fit to the continuum.

Table 8. Helium II 4686 Å.

Galaxy	FWHM 4686, Å	EW 4686, Å	Comment
(1)	(2)	(3)	(4)
40
108	2	0.38±0.06	narrow
178	7	0.45±0.13	...
182
218
242*	6	0.54±0.21	...
271*	no optical
298*
326*	no SDSS
1084*	10	1.19±0.04	broad + narrow
1567*	no SDSS
1578*	9	0.84±0.15	...
1637
1785
1942
2019
2021
2023
2110	no SDSS
2125	10	1.26±0.23	...
Min	2	0.38±0.06	...
Max	10	1.26±0.23	...

Note. — (1) KISSR ID. We mark the Ly α emitters with asterisks. (2) & (3) FWHM and EW of He II λ 4686 for galaxies with an SDSS spectrum and a 3σ detection. The last column indicates if the target has an optical spectrum or if a narrow He II emission component is present. The last two rows give the minimum and maximum values in each column.

We compared the observed values of $EW(\text{He II})$ with Starburst99 (Leitherer et al. 1999, 2010; Vázquez & Leitherer 2005) model predictions. Note that the observed values constitute lower limits due to the dilution of the He II line in the stellar continuum of older stellar generations. Table 8 lists $\text{FWHM}(\text{He II})$ and $EW(\text{He II})$. Figure 17 shows the comparison of observed and computed values of $EW(\text{He II})$ corresponding to single stellar populations (SSP) and continuous star formation (CSF) at the metallicities of the galaxies. Although Figure 17 shows that a given value of $EW(\text{He II})$ can be reached at multiple times, the range of times is restricted to $10^6 - 10^7$ yr for the SSP models, and $10^6 - 10^8$ yr for the CSF models. The presence of broad He II emission rules out an IMF deficient in massive stars or a population dominated by late-B and A stars. Therefore, according to the predictions by Charlot & Fall (1993) one would expect positive values of $EW(\text{Ly}\alpha)$ for the galaxies with broad He II emission. As previously mentioned, the lack of $\text{Ly}\alpha$ emission in KISSR 178 and KISSR 2125 is probably due to the dust geometry and inclination. In conclusion, we find no one to one correspondence between the $\text{Ly}\alpha$ emission and the presence of WR stars. This is in agreement with our age-dating analysis based on the N V profiles, where we concluded that some of the galaxies with young stellar populations are absorbers.

4. Discussion

4.1. $\text{Ly}\alpha$ and Gas Flows

Kunth et al. (1998) analyzed *HST*/GHRS observations of 8 nearby H II galaxies covering metallicities from $12+\log(\text{O}/\text{H})=8.0$ to solar, and reddenings from $E(\text{B}-\text{V})=0.1$ to 0.55. They found velocity offsets between the H I and the H II gas of up to 200 km s^{-1} in the four galaxies with $\text{Ly}\alpha$ emission (P-Cygni profiles), whereas they found broad damped $\text{Ly}\alpha$ absorptions at the velocity of the H II gas in galaxies with no signs of H I outflows from the LIS lines. These authors concluded that outflows are the main determining factor of the $\text{Ly}\alpha$ escape from galaxies. Our kinematical results are in very good agreement with these findings. However, one still needs to assess the relative importance of scattering in H I and destruction by dust on the $\text{Ly}\alpha$ escape.

We also find that the $\text{Ly}\alpha$ redshift is higher than the blueshift of the LIS lines by a factor of 1.5 – 2. This is in agreement with the high redshift observations of Shapley et al. (2003) and the expanding-shell radiation transport model of Verhamme et al. (2006).

Finally, note that the $\text{Ly}\alpha$ troughs are the result of a superposition of $\text{Ly}\alpha$ components. Therefore, the dominant component does not need to be at zero velocity. It is interesting that for our targets and for the targets in Kunth et al. (1998), the $\text{Ly}\alpha$ absorption centroid is consistent with the velocity of the H II gas.

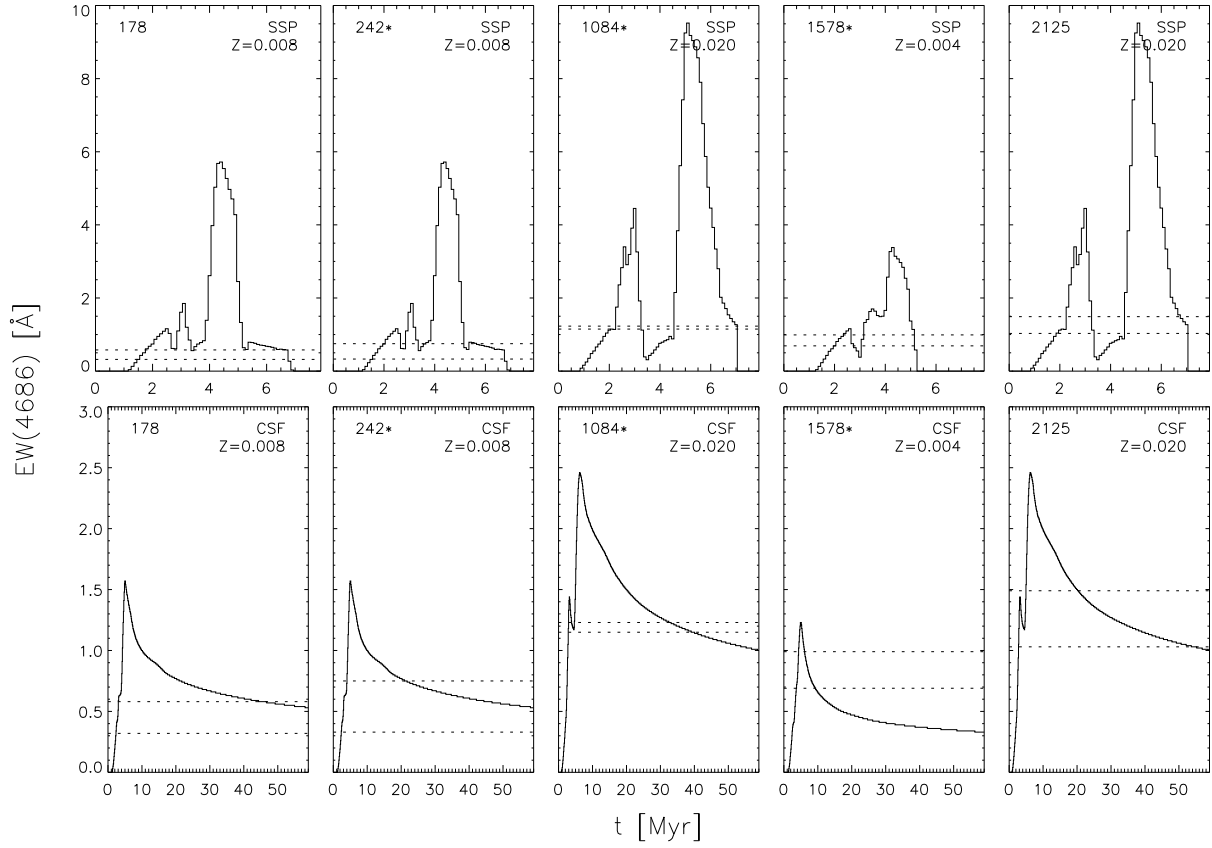


Fig. 17.— He II 4686 equivalent width versus time and metallicity for SSP (top) and CSF (bottom) models. In each panel, the dotted horizontal lines represent the upper and lower limits of $EW(\text{He II})$ for the galaxies with broad He II emission. We give the KISSR ID, SFH, and metallicity in each panel. The emitters are marked with asterisks.

4.2. KISSR 298

KISSR 298 is the double-peaked Ly α emitter. Such a profile is generally interpreted as a signature of Ly α radiation transfer through a non-static medium (see references given in section 4.5 of Verhamme et al. (2008)). For this object, we find an expansion velocity of 150 ± 47 km s $^{-1}$ from the LIS lines. This is high compared to the expansion velocities for the two double-peaked spectra in Verhamme et al. (2008), which are almost consistent with a static medium (they are < 25 km s $^{-1}$).

In KISSR 298, the blueshifted peak is twice as strong as the redshifted peak. Stronger blue peaks have been observed in star-forming galaxies at redshifts of $z = 2 - 3$ (Verhamme et al. 2007; Kulas et al. 2012). They are qualitatively consistent with an inflow (Verhamme et al. 2006) and could be due to in-falling gas originating in a galactic fountain, as in the model of Tenorio-Tagle (1996). The fact that in this system the dip between peaks essentially reaches the continuum is an interesting feature. Another possibility is that KISSR 298 has a broad Ly α emission line blended with an absorption, and that the absorption center is shifted redward. The shift could be caused by the relative motion of the emission region and the absorbing gas. A system corresponding to this description is shown in panel f of figure 3 of Wilman et al. (2005), which corresponds to the second cloud from the top in their figure 4. Unfortunately, the metal absorption lines of KISSR 298 are noisy and it is hard to tell if there are unexpected absorptions near the wavelength corresponding to the Ly α "absorption". As can be seen in Figure 11, the point equidistant to the two Ly α peaks of KISSR 298, which is marked with a dashed line, has a velocity coincident with the Si II 1304 and C II λ 1336 absorptions.

4.3. Ly α versus Aperture Size and Distance

We checked if there is an observational bias due to distance among the Ly α emitters in our sample. We excluded KISSR 1084 and 1567 from the analysis as one is of composite type and for the other the TA failed. In order to separate the effect of distance and metallicity/reddening, we divided the emitters in two sets: the low metallicity irregulars (KISSR 242, 1578, and 271) and the higher metallicity spirals (KISSR 298 and 326). Each set spans a factor of about 2 in distance (1.75 for the spirals and 1.7 for the irregulars). The spirals have low inclinations. Therefore the inclination angle is a secondary effect. We find that $L(1500)$, $EW(\text{Ly}\alpha)$, and $L(\text{Ly}\alpha)$ simultaneously increase with distance for both metallicity sets (see Table 6). Note that this result is based on small number statistics and that the general trend at much higher redshifts is that brighter objects have lower equivalent widths (e.g. Ando et al. 2006).

For the emitters, we find that $EW(\text{Ly}\alpha)$ is low compared to values determined in other studies at similar redshifts with larger apertures. Giavalisco et al. (1996) found that $EW(\text{Ly}\alpha) = 30$ Å on average for a sample of galaxies observed through the $10'' \times 20''$ aperture of *IUE*. We attribute this to our smaller aperture. Indeed, as previously mentioned, Östlin et al. (2009) found that in

nearby galaxies, the bulk of the $\text{Ly}\alpha$ emission is in the diffuse component of the galaxies. We also find that the emitters in our sample have $EW(\text{Ly}\alpha)$ slightly below the completeness limit of the $z = 0.3$ sample of Cowie et al. (2010), which is 15 \AA . However, our sample has a median absolute B magnitude of -19.4 (see Table 1), which is similar to that of the $z = 0.3$ sample (see their figure 23). This again could be an aperture effect. For Lyman-Break Galaxies (LBGs) at $z \sim 3$, the median value of $EW(\text{Ly}\alpha)$ is zero (see figure 8 of Shapley et al. 2003). Therefore, the EW s of the emitters in our sample are consistent with the latter median.

4.4. $\text{Ly}\alpha$ versus Metallicity/Reddening

If a homogeneous H I layer covers most of the H II region, the value of $EW(\text{Ly}\alpha)$ is expected to depend on the dust extinction because the $\text{Ly}\alpha$ line flux is more strongly reduced (due to multiple scattering effects) than the adjacent continuum.

Reddening due to the presence of dust is expected to increase with metallicity. We use oxygen as a gauge of metallicity. We re-derived the oxygen abundances of the 16 galaxies with SDSS spectra using the method described in Salzer et al. (2005). In summary, in cases where the weak [O III] $\lambda 4363$ line was not detected, we used the mean of the oxygen abundances derived from the EP and SDSS COARSE calibrations, and in cases where the R23 abundance could be computed, we used the mean of the EP, SDSS and R23 abundances (all methods are defined in Salzer et al. 2005). The oxygen abundances from the KISSR and the SDSS data are in agreement within the uncertainties and the final values are those given in Table 1.

We find that the two most metal-poor and least reddened galaxies, KISSR 2019 and 2110, show $\text{Ly}\alpha$ in pure absorption, while the most metal-rich and most reddened galaxy, KISSR 298, has the highest value of $EW(\text{Ly}\alpha)$. Strong $\text{Ly}\alpha$ emission is expected from KISSR 2019 and 2110 based on the strength of their N V profiles and their high values of $EW(H\alpha)$ ($\sim 500 \text{ \AA}$), which are characteristic of a young burst of star formation. However, these two targets show $\text{Ly}\alpha$ in absorption. This is not surprising given that this is also the case for I Zw 18, the most metal-poor galaxy in the local universe (Atek et al. 2009). Although we suffer from small number statistics, the lack of one to one correspondence between the strength of $\text{Ly}\alpha$ and metallicity/reddening is in agreement with the work of Giavalisco et al. (1996), which is based on larger optical and ultraviolet apertures than what we use in the present study. Therefore, it is not clear that larger aperture measurements yield a different result regarding $\text{Ly}\alpha$ versus metallicity. Our upcoming $\text{Ly}\alpha$ plus $H\alpha/H\beta$ ratio maps of three of the galaxies in our sample should help establish the role of dust and metallicity in regulating the $\text{Ly}\alpha$ escape. These maps will be obtained as part of *HST* GO-12951 and will enable the measurement of spatially resolved and integrated $\text{Ly}\alpha$ and reddening values.

5. SUMMARY AND CONCLUSION

1. We used the *HST* COS to observe 20 nearby ($z \sim 0.03$) galaxies spanning a broad range in properties (Table 1). Our data covers the wavelength range $1138 - 1457 \text{ \AA}$ and samples circular regions of 0.9-2.4 kpc in radius within each galaxy. We studied correlations between the Ly α line properties and galaxy properties including distance, metallicity, reddening, starburst phase, and gas flow properties. Our study includes the analysis of ancillary optical spectroscopy from SDSS and KISS. Based on the BPT diagram (Figure 1), the galaxies are dominated by star-formation except for KISSR 1084, which is of composite spectral type.
2. We found Ly α profile shapes representative of what has been observed between redshifts of $z \sim 0$ and $z \sim 5$ (e.g., Kunth et al. 1998; Tapken et al. 2007; Kulas et al. 2012), including strong absorptions, P-Cygni profiles with redshifted emission, and double emission (Figure 10).
3. Seven out of the 20 galaxies have net Ly α emission, including spiral and irregular galaxies and composite galaxy KISSR 1084 (Figures 3 and 10). For these seven emitters, the Ly α equivalent width is in the range $1 - 12 \text{ \AA}$ and the range of escape fractions within the COS aperture is $1 - 12 \%$ (Table 6). The comparison with escape fractions at higher redshifts is complicated by the fact that at higher redshifts, observations include more if not all of the galaxy in the aperture.
4. A face-on spiral, KISSR 298, shows two peaks of Ly α emission separated by 370 km s^{-1} , one blueshifted and one redshifted and half as strong. Unfortunately, we were unable to determine if this profile is a strong emission with absorption within, as LIS lines for this galaxy are too noisy.
5. Excluding KISSR 298, the emitters have Ly α peaks redshifted to $172 \pm 49 \text{ km s}^{-1}$ with respect to H α (mean \pm standard deviation). Including all emitters, the mean O I $\lambda 1302$ and C II $\lambda 1334$ absorption blueshifts are -117 ± 47 and $-94 \pm 20 \text{ km s}^{-1}$. Therefore, excluding KISSR 298, the Ly α redshift is larger than the interstellar absorption blueshift by approximately a factor of 1.5–2, as found at high redshift (e.g. Shapley et al. 2003), and in agreement with radiation transfer models (e.g., Verhamme et al. 2006).
6. For the absorbers, Ly α is centered at $0 \pm 38 \text{ km s}^{-1}$ and O I and C II have centroids at -23 ± 28 and $-21 \pm 31 \text{ km s}^{-1}$. Thus, most absorbers are consistent with having static or low velocity H I gas. This supports earlier findings (e.g. of Kunth et al. 1998).
7. The outflow velocity of Si III $\lambda 1206$ is typically, $30 - 50 \text{ km s}^{-1}$ greater than that of the H I gas (Table 5).
8. We found no one to one correspondence between the strength of Ly α and the reddening/metallicity measured within the COS aperture (Tables 6 and 7). In particular, we found three low-inclination spirals each showing different Ly α profiles, i.e., pure absorption, double

emission, and P-Cygni profile, and the two most metal-poor and least-reddened galaxies in our sample are pure absorbers.

9. We find stellar populations consistent with SSPs of ages in the range 5-10 Myr among the Ly α emitters and the Ly α absorbers. Similarly, we detect signatures of the presence of Wolf-Rayet stars among the emitters and the absorbers. Therefore, a young starburst does not guarantee strong Ly α emission.
10. In conclusion, a picture emerges where the Ly α photons escape through regions of low H I and dust column densities, where gas outflows are occurring.
11. In *HST* cycle 20, we will map three low-inclination spirals from our sample in the Ly α line and the H β /H α ratio (proxy for dust attenuation). This will make it possible to study the relative importance of gas flows and dust content in regulating the Ly α escape.

6. Acknowledgments

Support for this work has been provided by NASA through an award to University of Colorado (Boulder) entitled "Cosmic Origins Spectrograph GTO". Award number NNX08AC14G. We thank C. Danforth, K. France, and J. Tumlinson for their codes, which were used for reducing (CD) and analyzing (KF and JT) the COS data. We also thank C. Thom for his help with the H I 21 cm data, and Z. Zheng for helpful comments regarding the Ly α profile of KISSR 298. Finally, we thank the referee for comments that have helped to greatly improve this paper.

REFERENCES

- Abazajian, K. N., et al. 2009, ApJS, 182, 543
- Ando, M., Ohta, K., Iwata, I., Akiyama, M., Aoki, K., & Tamura, N. 2006, ApJ, 645, L9
- Asplund, M., Grevesse, N., Sauval, A. J., & Scott, P. 2009, ARA&A, 47, 481
- Atek, H., Schaerer, D., & Kunth, D. 2009, A&A, 502, 791
- Bastian, N., Covey, K. R., & Meyer, M. R. 2010, ARA&A, 48, 339
- Beals, C. S. 1929, MNRAS, 90, 202
- Bibby, J. L., & Crowther, P. A. 2012, MNRAS, 420, 3091
- Bouret, J.-C., Hillier, D. J., Lanz, T., & Fullerton, A. W. 2012, A&A, 544, A67
- Bouwens, R. J., Illingworth, G. D., Franx, M., & Ford, H. 2007, ApJ, 670, 928

- Bouwens, R. J., et al. 2011a, *Nature*, 469, 504
- . 2011b, *ApJ*, 737, 90
- Bradač, M., et al. 2012, *ApJ*, 755, L7
- Calzetti, D., Armus, L., Bohlin, R. C., Kinney, A. L., Koornneef, J., & Storchi-Bergmann, T. 2000, *ApJ*, 533, 682
- Calzetti, D., & Kinney, A. L. 1992, *ApJ*, 399, L39
- Chandar, R., Leitherer, C., Tremonti, C., & Calzetti, D. 2003, *ApJ*, 586, 939
- Charlot, S., & Fall, S. M. 1993, *ApJ*, 415, 580
- Conti, P. S. 1991, *ApJ*, 377, 115
- Cowie, L. L., Barger, A. J., & Hu, E. M. 2010, *ApJ*, 711, 928
- Cowie, L. L., & Hu, E. M. 1998, *AJ*, 115, 1319
- Danforth, C. W., Keeney, B. A., Stocke, J. T., Shull, J. M., & Yao, Y. 2010, *ApJ*, 720, 976
- Dawson, S., Rhoads, J. E., Malhotra, S., Stern, D., Wang, J., Dey, A., Spinrad, H., & Jannuzi, B. T. 2007, *ApJ*, 671, 1227
- Eldridge, J. J., Izzard, R. G., & Tout, C. A. 2008, *MNRAS*, 384, 1109
- Finkelstein, S. L., Rhoads, J. E., Malhotra, S., & Grogin, N. 2009, *ApJ*, 691, 465
- Finkelstein, S. L., Rhoads, J. E., Malhotra, S., Grogin, N., & Wang, J. 2008, *ApJ*, 678, 655
- Fitzpatrick, E. L. 1999, *PASP*, 111, 63
- Fujita, A., Martin, C. L., Mac Low, M.-M., & Abel, T. 2003, *ApJ*, 599, 50
- Gawiser, E., et al. 2007, *ApJ*, 671, 278
- Giavalisco, M. 2002, *ARA&A*, 40, 579
- Giavalisco, M., Koratkar, A., & Calzetti, D. 1996, *ApJ*, 466, 831
- González, J. E., Lacey, C. G., Baugh, C. M., Frenk, C. S., & Benson, A. J. 2012, *MNRAS*, 423, 3709
- Grevesse, N., & Sauval, A. J. 1998, *Space Sci. Rev.*, 85, 161
- Gronwall, C., et al. 2007, *ApJ*, 667, 79
- Hu, E. M., Cowie, L. L., Barger, A. J., Capak, P., Kakazu, Y., & Trouille, L. 2010, *ApJ*, 725, 394

- Hu, E. M., Cowie, L. L., Capak, P., McMahon, R. G., Hayashino, T., & Komiyama, Y. 2004, *AJ*, 127, 563
- Hu, E. M., Cowie, L. L., & McMahon, R. G. 1998, *ApJ*, 502, L99
- Iye, M., et al. 2006, *Nature*, 443, 186
- Jangren, A., Salzer, J. J., Sarajedini, V. L., Gronwall, C., Werk, J. K., Chomiuk, L., Moody, J. W., & Boroson, T. A. 2005, *AJ*, 130, 2571
- Kalberla, P. M. W., Burton, W. B., Hartmann, D., Arnal, E. M., Bajaja, E., Morras, R., & Pöppel, W. G. L. 2005, *A&A*, 440, 775
- Kashikawa, N., et al. 2006, *ApJ*, 648, 7
- Kauffmann, G., et al. 2003, *MNRAS*, 346, 1055
- Kennicutt, Jr., R. C. 1998, *ARA&A*, 36, 189
- Kewley, L. J., Dopita, M. A., Sutherland, R. S., Heisler, C. A., & Trevena, J. 2001, *ApJ*, 556, 121
- Kewley, L. J., Groves, B., Kauffmann, G., & Heckman, T. 2006, *MNRAS*, 372, 961
- Kriss, G. A., et al. 2011, *A&A*, 534, A41
- Kroupa, P. 2001, *MNRAS*, 322, 231
- Kudritzki, R.-P., et al. 2000, *ApJ*, 536, 19
- Kulas, K. R., Shapley, A. E., Kollmeier, J. A., Zheng, Z., Steidel, C. C., & Hainline, K. N. 2012, *ApJ*, 745, 33
- Kunth, D., Mas-Hesse, J. M., Terlevich, E., Terlevich, R., Lequeux, J., & Fall, S. M. 1998, *A&A*, 334, 11
- Leitherer, C., Ortiz Otálvaro, P. A., Bresolin, F., Kudritzki, R.-P., Lo Faro, B., Pauldrach, A. W. A., Pettini, M., & Rix, S. A. 2010, *ApJS*, 189, 309
- Leitherer, C., et al. 1999, *ApJS*, 123, 3
- Levesque, E. M., Leitherer, C., Ekstrom, S., Meynet, G., & Schaerer, D. 2012, *ApJ*, 751, 67
- López-Sánchez, Á. R., & Esteban, C. 2010, *A&A*, 516, A104
- Maeder, A., Grebel, E. K., & Mermilliod, J.-C. 1999, *A&A*, 346, 459
- Maeder, A., & Meynet, G. 1994, *A&A*, 287, 803
- Malhotra, S., & Rhoads, J. E. 2002, *ApJ*, 565, L71

- . 2006, *ApJ*, 647, L95
- Malhotra, S., Rhoads, J. E., Finkelstein, S. L., Hathi, N., Nilsson, K., McLinden, E., & Pirzkal, N. 2012, *ApJ*, 750, L36
- Martin, D. C., et al. 2005, *ApJ*, 619, L1
- McCall, M. L., Rybski, P. M., & Shields, G. A. 1985, *ApJS*, 57, 1
- Meynet, G., & Maeder, A. 2005, *A&A*, 429, 581
- Meynet, G., Maeder, A., Schaller, G., Schaerer, D., & Charbonnel, C. 1994, *A&AS*, 103, 97
- Nilsson, K. K. 2007, ArXiv e-prints, 0711.2199
- Nilsson, K. K., Tapken, C., Møller, P., Freudling, W., Fynbo, J. P. U., Meisenheimer, K., Laursen, P., & Östlin, G. 2009, *A&A*, 498, 13
- Nilsson, K. K., et al. 2007, *A&A*, 471, 71
- Oesch, P. A., et al. 2010, *ApJ*, 709, L16
- Osterbrock, D. E., & Ferland, G. J. 2006, *Astrophysics of gaseous nebulae and active galactic nuclei*
- Osterman, S., et al. 2011, *Ap&SS*, 335, 257
- Östlin, G., Hayes, M., Kunth, D., Mas-Hesse, J. M., Leitherer, C., Petrosian, A., & Atek, H. 2009, *AJ*, 138, 923
- Ota, K., Richard, J., Iye, M., Shibuya, T., Egami, E., & Kashikawa, N. 2012, *MNRAS*, 423, 2829
- Ouchi, M., et al. 2001, *ApJ*, 558, L83
- . 2003, *ApJ*, 582, 60
- . 2004, *ApJ*, 611, 660
- . 2005, *ApJ*, 620, L1
- . 2008, *ApJS*, 176, 301
- Partridge, R. B., & Peebles, P. J. E. 1967, *ApJ*, 147, 868
- Rhoads, J. E., Malhotra, S., Dey, A., Stern, D., Spinrad, H., & Jannuzi, B. T. 2000, *ApJ*, 545, L85
- Rhoads, J. E., et al. 2003, *AJ*, 125, 1006
- Salzer, J. J., Lee, J. C., Melbourne, J., Hinz, J. L., Alonso-Herrero, A., & Jangren, A. 2005, *ApJ*, 624, 661

- Salzer, J. J., et al. 2001, *AJ*, 121, 66
- Scarlata, C., et al. 2009, *ApJ*, 704, L98
- Schaerer, D. 2007, *ArXiv e-prints*, 0706.0139
- Schaller, G., Schaerer, D., Meynet, G., & Maeder, A. 1992, *A&AS*, 96, 269
- Schlegel, D. J., Finkbeiner, D. P., & Davis, M. 1998, *ApJ*, 500, 525
- Shapley, A. E. 2011, *ARA&A*, 49, 525
- Shapley, A. E., Steidel, C. C., Pettini, M., & Adelberger, K. L. 2003, *ApJ*, 588, 65
- Shimasaku, K., et al. 2006, *PASJ*, 58, 313
- Shirazi, M., & Brinchmann, J. 2012, *MNRAS*, 421, 1043
- Steidel, C. C., Adelberger, K. L., Shapley, A. E., Pettini, M., Dickinson, M., & Giavalisco, M. 2003, *ApJ*, 592, 728
- Steidel, C. C., Giavalisco, M., Pettini, M., Dickinson, M., & Adelberger, K. L. 1996, *ApJ*, 462, L17
- Stiavelli, M., et al. 2005, *ApJ*, 622, L1
- Tanaka, M. 2012, *PASJ*, 64, 37
- Taniguchi, Y., et al. 2005, *PASJ*, 57, 165
- Tapken, C., Appenzeller, I., Noll, S., Richling, S., Heidt, J., Meinköhn, E., & Mehlert, D. 2007, *A&A*, 467, 63
- Tenorio-Tagle, G. 1996, *AJ*, 111, 1641
- Tremonti, C. A., Calzetti, D., Leitherer, C., & Heckman, T. M. 2001, *ApJ*, 555, 322
- Valls-Gabaud, D. 1993, *ApJ*, 419, 7
- Vázquez, G. A., & Leitherer, C. 2005, *ApJ*, 621, 695
- Venemans, B. P., et al. 2002, *ApJ*, 569, L11
- . 2004, *A&A*, 424, L17
- . 2005, *A&A*, 431, 793
- Verhamme, A., Schaerer, D., Atek, H., & Tapken, C. 2007, in *Astronomical Society of the Pacific Conference Series*, Vol. 380, *Deepest Astronomical Surveys*, ed. J. Afonso, H. C. Ferguson, B. Mobasher, & R. Norris, 97

- Verhamme, A., Schaerer, D., Atek, H., & Tapken, C. 2008, *A&A*, 491, 89
- Verhamme, A., Schaerer, D., & Maselli, A. 2006, *A&A*, 460, 397
- Wang, J. X., Malhotra, S., & Rhoads, J. E. 2005, *ApJ*, 622, L77
- Wilman, R. J., Gerssen, J., Bower, R. G., Morris, S. L., Bacon, R., de Zeeuw, P. T., & Davies, R. L. 2005, *Nature*, 436, 227
- Wofford, A., Leitherer, C., & Chandar, R. 2011, *ApJ*, 727, 100
- York, D. G., et al. 2000, *AJ*, 120, 1579
- Zheng, Z., Cen, R., Trac, H., & Miralda-Escudé, J. 2010, *ApJ*, 716, 574
- Zheng, Z.-Y., et al. 2012, *ApJ*, 746, 28